The Astrophysical Journal Supplement Series, 236:52 (25pp), 2018 June https://doi.org/10.3847/1538-4365/aabfe9

Chemical Survey toward Young Stellar Objects in the Perseus Molecular Cloud Complex

Aya E. Higuchi[1], Nami Sakai[1], Yoshimasa Watanabe[2], Ana López-Sepulcre[3,4], Kento Yoshida[1,5], Yoko Oya[5], Muneaki Imai[5], Yichen Zhang[1], Cecilia Ceccarelli[3], Bertrand Lefloch[3], Claudio Codella[6], Rafael Bachiller[7], Tomoya Hirota[8], Takeshi Sakai[9], and Satoshi Yamamoto[5]

[1] RIKEN Cluster for Pioneering Research, 2-1, Hirosawa, Wako-shi, Saitama 351-0198, Japan; aya.higuchi@riken.jp
[2] Division of Physics, Faculty of Pure and Applied Sciences, University of Tsukuba, Tsukuba, Ibaraki 305-8571, Japan
[3] Univ. Grenoble Alpes, CNRS, Institut de Plan étologie et d'Astrophysique de Grenoble (IPAG), F-38000 Grenoble, France
[4] Institut de Radioastronomie Millimétrique, 300 rue de la Piscine, Domaine Universitaire de Grenoble, F-38406 Saint-Martin d'H ères, France
[5] Department of Physics, The University of Tokyo, Hongo, Bunkyo-ku, Tokyo 113-0033, Japan
[6] INAF, Osservatorio Astrofisico di Arcetri, Largo E. Fermi 5, I-50125, Firenze, Italy
[7] IGN Observatorio Astronómico Nacional, Apartado 1143, E-28800 Alcalá de Henares, Spain
[8] National Astronomical Observatory of Japan, Osawa, Mitaka, Tokyo 181-8588, Japan
[9] Department of Communication Engineering and Informatics, Graduate School of Informatics and Engineering, The University of Electro-Communications, Chofugaoka, Chofu, Tokyo 182-8585, Japan

Received 2017 December 1; revised 2018 April 20; accepted 2018 April 21; published 2018 June 20

Abstract

The chemical diversity of gas in low-mass protostellar cores is widely recognized. In order to explore the origin of this diversity, a survey of chemical composition toward 36 Class 0/I protostars in the Perseus molecular cloud complex, which are selected in an unbiased way under certain physical conditions, has been conducted with IRAM 30 m and NRO 45 m telescope. Multiple lines of C_2H, c-C_3H_2, and CH_3OH have been observed to characterize the chemical composition averaged over a 1000 au scale around the protostar. The derived beam-averaged column densities show significant chemical diversity among the sources, where the column density ratios of C_2H/CH_3OH are spread out by two orders of magnitude. From previous studies, the hot corino sources have abundant CH_3OH but deficient C_2H, their C_2H/CH_3OH column density ratios being relatively low. In contrast, the warm-carbon-chain chemistry (WCCC) sources are found to reveal the high C_2H/CH_3OH column density ratios. We find that the majority of the sources have intermediate characters between these two distinct chemistry types. A possible trend is seen between the C_2H/CH_3OH ratio and the distance of the source from the edge of a molecular cloud. The sources located near cloud edges or in isolated clouds tend to have a high C_2H/CH_3OH ratio. On the other hand, the sources having a low C_2H/CH_3OH ratio tend to be located in the inner regions of the molecular cloud complex. This result gives an important clue toward understanding the origin of the chemical diversity of protostellar cores in terms of environmental effects.

Key words: astrochemistry – ISM: molecules – stars: formation – stars: low-mass

Supporting material: extended figures

1. Introduction

The chemical compositions of protostellar cores are of fundamental importance because they are related to the initial condition for chemical evolution toward protoplanetary disks. During the last decade, they have extensively been studied by radioastronomical observations. Now, it is well known that the chemical compositions of low-mass protostellar cores ($r < \sim$1000 au) show significant diversity (Sakai & Yamamoto 2013). One distinct case of diversity is hot corino chemistry. It is characterized by rich complex-organic molecules (COMs) such as $HCOOCH_3$ and $(CH_3)_2O$, and deficient carbon-chain molecules such as C_2H, c-C_3H_2 and C_4H. A prototypical hot corino source is IRAS 16293-2422 (e.g., Cazaux et al. 2003; Bottinelli et al. 2004). Another distinct case is warm-carbon-chain chemistry (WCCC). It is characterized by abundant carbon-chain molecules and deficient COMs. A prototypical WCCC source is IRAS 04368+2557 in L1527 (Sakai et al. 2008). This kind of exclusive chemical feature between COMs and carbon-chain molecules represents a major axis of chemical diversity. It should be noted that we do not know at this moment whether any other axes exist. In this paper, we therefore use the word "chemical diversity" to represent the hot corino chemistry versus WCCC axis.

Sakai et al. (2009) proposed that one possible origin of the above chemical diversity of low-mass protostellar cores is the difference of the duration time of their starless phase after the shielding of the interstellar UV radiation. After the UV-shielding, the formation of molecules starts both in the gas-phase and on dust grains, whose timescale is comparable to the dynamical timescale of a parent cloud (i.e., free-fall time). A longer duration for the starless phase tends to result in hot corino chemistry, while a shorter duration time results in WCCC. This mechanism can explain the various observational results obtained so far (Sakai & Yamamoto 2013). For instance, lower deuterium fractionation ratios and association of young starless cores near the WCCC source are consistent with this picture (Sakai et al. 2010; Sakai & Yamamoto 2013). However, other mechanisms such as shocks (outflows, cloud–cloud/filament–filament collision) and UV radiation from nearby OB stars may also contribute to chemical diversity (e.g., Buckle & Fuller 2002; Higuchi et al. 2010, 2014;

Lindberg & Jørgensen 2012; Watanabe et al. 2012; Fukui et al. 2015; Spezzano et al. 2016a, 2016b). Hence, the origin of the above chemical diversity is still controversial.

So far, only a few sources have unambiguously been identified as hot corino sources and WCCC sources each. Examples of the former are IRAS 16293-2422, NGC 1333 IRAS 4A, NGC 1333 IRAS 4B, NGC 1333 IRAS 2, Serpens SMM1, Serpens SMM4, and HH212 (e.g., Cazaux et al. 2003; Bottinelli et al. 2004; Sakai et al. 2006; Öberg et al. 2011; Codella et al. 2016). Examples of the latter are L1527, IRAS 15398-3359, and TMC-1A (e.g., Sakai et al. 2008, 2014a). Thus, the statistics is very poor. To improve our understanding of the origin of the chemical diversity of protostellar cores, we need to know what kind of chemistry is commonly occurs. Recently, Lindberg et al. (2016) and Graninger et al. (2016) reported statistical studies of the CH_3OH and C_4H abundances toward low-mass star-forming cores. They used CH_3OH and C_4H as representative COM and carbon-chain molecules, respectively. Although these studies provide us with rich information on chemical diversity, different distances to the sources, as well as regional differences in physical conditions (UV radiation field, star formation activities) may complicate an interpretation of the observed chemical diversity.

A powerful approach to overcoming this situation is an unbiased survey of all protostellar cores in a single molecular cloud complex. Such a study would allow us to explore environmental effects on the chemical composition of protostellar sources in the molecular cloud complex without any preconception. In addition, all the targets are at almost the same distance, and are therefore affected similarly by beam dilution effects. This feature makes statistical arguments easier. With these in mind, we have conducted an unbiased chemical survey of the Perseus molecular cloud complex in the 3 and 1.3 mm bands. We observed the CH_3OH lines as a proxy of the COMs, because CH_3OH is a parent molecule for the production of larger COMs. We employed the C_2H and c-C_3H_2 lines as a proxy of carbon-chain-related molecules, because they are the most fundamental carbon-chain molecules giving bright emission. By comparing the results for these molecules, we discuss the chemical diversity of protostellar cores in Perseus.

2. Observations

2.1. Observed Sources and Molecules

The Perseus molecular cloud complex is one of the most famous and well-studied nearby low-mass star-forming regions (e.g., Hatchell et al. 2005; Jørgensen et al. 2006). The distance from the Sun is reported to be 235–238 pc (Hirota et al. 2008, 2011). In this paper, we employ a distance of 235 pc. It consists of a few molecular clouds, including NGC 1333, L1455, L1448, IC 348, B1, and Barnard 5 (B5), which show different star formation activities. In the whole Perseus molecular cloud extending over a 10 pc scale, about 400 sources are identified as young stellar object candidates, among which more than 50 are thought to be Class 0 or Class I protostars (Hatchell et al. 2005). We selected the target sources from the list by Hatchell et al. (2007) under the following criteria. (1) The protostellar sources are in the Class 0/I stage. (2) The bolometric luminosity is higher than 1 $L_\odot$ (except for B1-5; 0.7 $L_\odot$). (3) The envelope mass is higher than 1 $M_\odot$ to ensure association of a substantial amount of molecular gas. In total, 36 protostellar sources are in our target-source list (Table 1). Our sample is unbiased under the above three conditions. It should be stressed that it is unbiased from the viewpoint of chemical conditions.

Table 1
Source List

IDs	Source Names	R.A. (J2000)	Decl. (J2000)
NGC 1333-1	IRAS 4B	03:29:12.01	31:13:08.2
NGC 1333-2	IRAS 2A	03:28:55.57	31:14:37.1
NGC 1333-3	IRAS 6; SK-24	03:29:01.66	31:20:28.5
NGC 1333-4	IRAS 7; SK-20	03:29:10.72	31:18:20.5
NGC 1333-5	IRAS 4C; SK-5	03:29:13.62	31:13:57.9
NGC 1333-6	IRAS 1; SK-6	03:28:37.11	31:13:28.3
NGC 1333-7	HH7-11 MMS 1; SK-15	03:29:06.50	31:15:38.6
NGC 1333-8	HH7-11 MMS 6; SK-14	03:29:04.09	31:14:46.6
NGC 1333-9	SVS 3; SK-28	03:29:10.70	31:21:45.3
NGC 1333-10	SK-29	03:29:07.70	31:21:56.8
NGC 1333-11	SK-18	03:29:07.10	31:17:23.7
NGC 1333-12	SK-32	03:29:18.25	31:23:16.9
NGC 1333-13		03:29:19.70	31:23:56.0
NGC 1333-14	No SMM/MM source	03:28:56.20	31:19:12.5
NGC 1333-15	SK-22	03:29:15.30	31:20:31.2
NGC 1333-16	IRAS 4A	03:29:10.53	31:13:31.0
NGC 1333-17	SVS 13A	03:29:03.75	31:16:03.76
L1448-1	L1448 NW; IRS3C	03:25:35.66	30:45:34.2
L1448-2	L1448 NB; IRS3	03:25:36.33	30:45:14.8
L1448-3	L1448 MM	03:25:38.87	30:44:05.3
L1448-4	IRS2	03:25:22.38	30:45:13.3
L1448-5	IRS2E	03:25:25.90	30:45:02.7
IC 348-1	HH211	03:43:56.80	32:00:50.3
IC 348-2	IC 348 MMS	03:43:57.05	32:03:05.0
IC 348-3		03:44:43.32	32:01:31.6
IC 348-4		03:43:50.99	32:03:24.7
Barnard 5	IRS 1	03:47:41.61	32:51:43.9
B1-1	B1-c	03:33:17.87	31:09:32.3
B1-2	B1-d	03:33:16.49	31:06:52.3
B1-3	B1-a	03:33:16.67	31:07:55.1
B1-4		03:32:18.03	30:49:46.9
B1-5		03:31:20.94	30:45:30.3
L1455-1	IRAS 03235+3004	03:26:37.46	30:15:28.2
L1455-2	IRS1; RNO 15 FIR; IRAS 03245+3002	03:27:39.11	30:13:02.8
L1455-3	IRS4	03:27:43.25	30:12:28.9
L1455-4	IRS2	03:27:47.69	30:12:04.4

Note. All sources are listed in Hatchell et al. (2005). A distance of 235 pc is adopted for all the sources.

We observed the CH_3OH, C_2H, and c-C_3H_2 lines listed in Table 2. CH_3OH is the most fundamental saturated organic molecule that is abundant in hot corino sources (e.g., Maret et al. 2005; Kristensen et al. 2010; Sakai et al. 2012). On the other hand, C_2H and c-C_3H_2 are basic carbon-chain-related molecules that are abundant in WCCC sources (e.g., Sakai et al. 2008, 2009). Hence, we can characterize the chemical composition of the sources with these species.

2.2. Observation with the Nobeyama 45 m Telescope

Observations of the CH_3OH lines in the 3 mm band were carried out with the 45 m telescope at the Nobeyama Radio Observatory (NRO) during 2014 January and 2015 March toward the target sources, except for NGC 1333-16 (IRAS 4A) and NGC 1333-17 (SVS 13A). These two sources were not observed due to the limited observation time. The side-band-separating (2SB) mixer receiver T100HV was used

Table 2
List of Observed Molecules

Molecule	Transition	Frequency (GHz)	E_u (K)	$S\mu^2$ (D^2)
C_2H	$N = 3–2, J = 5/2–3/2, F = 2–1$	262.06746	25.2	1.1
	$N = 3–2, J = 5/2–3/2, F = 3–2$	262.06498	25.2	1.6
	$N = 3–2, J = 7/2–5/2, F = 3–2$	262.00648	25.1	1.7
	$N = 3–2, J = 7/2–5/2, F = 4–3$	262.00426	25.2	2.3
CH_3OH	$J = 5–4, K = 2\ E^-$	241.90415	60.8	3.4
	$J = 5–4, K = 2\ A^+$	241.88770	72.6	3.4
	$J = 5–4, K = 1\ E^+$	241.87907	55.9	4.0
	$J = 5–4, K = 3\ E^-$	241.85235	97.6	2.6
	$J = 5–4, K = 2\ A^-$	241.84232	72.5	3.4
	$J = 5–4, K = 3\ A^\pm$	241.83291	84.7	2.6
	$J = 5–4, K = 4\ E^+$	241.82964	130.8	1.5
	$J = 5–4, K = 4\ E^-$	241.81325	122.7	1.4
	$J = 5–4, K = 4\ A^\pm$	241.80650	115.2	1.5
	$J = 5–4, K = 0\ A^+$	241.79143	34.8	4.0
	$J = 5–4, K = 1\ E^-$	241.76722	40.4	3.9
	$J = 5–4, K = 0\ E^+$	241.70021	47.9	4.0
CH_3OH	$J = 2–1, K = 0\ E^+$	96.74455	20.1	1.6
	$J = 2–1, K = 0\ A^+$	96.74137	7.0	1.6
	$J = 2–1, K = 1\ E^-$	96.73936	12.5	1.2
c-C_3H_2	$3_{2,1}–2_{1,2}$ (ortho)	244.22216	18.2	7.3

as the front end, with the typical system noise temperature ranging from 150 to 200 K. The beam size (HPBW) is 21″ at 90 GHz, which corresponds to 4900 au at a distance of 235 pc. The back-end was a bank of 16 SAM-45 auto-correlators, whose bandwidth and frequency resolution each are 250 MHz and 122 kHz (with a velocity resolution of ∼0.4 km s^{-1}), respectively.

The telescope pointing was checked every hour by observing the SiO maser source, NML Tau. The pointing accuracy was confirmed to be better than 7″. The position switching mode was employed for all the above sources, where the position with the $C^{18}O$ integrated intensity lower than 1 K km s^{-1} (Hatchell et al. 2005) near each target molecular cloud is taken as the off-position. The offset of the off-position relative to the target-source position is (δR.A., δdecl.) = (−1200″, 0″) for the sources in the NGC 1333 region, (−600″, 0″) for the sources in the L1448 region, (−600″, 0″) for the sources in the IC 348 and the Barnard 5 regions, (−850″, 0″) for the sources in the B1 region, and (0″, 780″) for the sources in the L1455 region. The intensity scale was calibrated to the antenna temperature (T_A^*) scale using the chopper-wheel method. The antenna temperature was converted to the main-beam brightness temperature using the main-beam efficiency of 0.45 provided by the observatory. The uncertainty of the intensity calibration is estimated to be better than 20%. The observed data were reduced with the software package NEWSTAR developed at NRO.

2.3. Observation with the IRAM 30 m Telescope

Observations of the CH_3OH, C_2H, and c-C_3H_2 lines in the 1.3 mm band were carried out with the Institut de Radio Astronomie Millimétrique (IRAM) 30 m telescope at Pico Veleta. The sources, except for NGC 1333-16 (IRAS 4A) and NGC 1333-17 (SVS 13A), were observed in the period from between 2015 January to 2016 May. For these two sources, we use the data taken by the ASAI (Astrochemical Survey At IRAM) project (Lefloch et al. 2018). The Eight Mixer Receiver (EMIR), E230, was employed in the dual-polarization mode. The system temperatures ranged from 250 to 400 K. HPBW is 10″ at 260 GHz, which corresponds to 2400 au at a distance of 235 pc. The back-end consists of eight Fourier transform spectrometers (FTS), whose bandwidth and channel width each are 400 MHz and 200 kHz (with a velocity resolution of ∼0.3 km s^{-1}), respectively. The telescope pointing was checked every hour by observing nearby continuum sources and was confirmed to be better than ∼5″. The position switching mode was employed for all the above sources. As for the off-position, we used the same position used for the Nobeyama observations, while the wobbler switching mode was employed for NGC 1333-16 and NGC 1333-17.[10] The intensity scale was calibrated to the antenna temperature scale using the two temperature loads. T_A^* was then converted to the main-beam temperature T_{MB} by multiplying F_{eff}/B_{eff} (mean value between 240 and 260 GHz), where F_{eff} is the forward efficiency (0.92) and B_{eff} is the main-beam efficiency (0.59). The uncertainty of the intensity calibration is estimated to be better than 20%. The data were reduced with the CLASS software of the GILDAS package.

3. Results

3.1. Data Analyses

Figure 1 shows the observed spectral lines of CH_3OH ($J = 5–4, K = 1, E^-, E_u = 40$ K) and C_2H ($N = 3–2, J = 5/2–3/2, F = 3–2, E_u = 25$ K) for a few selected sources. The relative intensities between CH_3OH and C_2H are significantly different among the sources (see Table 3). For instance, the CH_3OH line is strongly detected toward NGC 1333-1, whereas the intensity of the C_2H line is weak. In contrast, NGC 1333-6 shows an opposite trend; CH_3OH is not detected. A similar trend can be seen in B1-5: the C_2H lines are strong, while the CH_3OH lines are weak. For B1-3 and L1448-3, both the CH_3OH and C_2H lines are moderately intense. To quantify the trend, we evaluated the line parameters for each line by assuming that the line profile is approximated by a Gaussian function.

The CH_3OH lines at 242 GHz would likely trace a relatively dense and warm region rather than a cold ambient cloud, because of their upper state energies (e.g., CH_3OH; $J = 5–4, K = 1, E^-, E_u = 40$ K) and their critical densities ($10^{5–6}$ cm^{-3}). The CH_3OH ($J = 5–4$) lines were detected toward 35 of the 36 sources. Their spectra are shown in Figure 2. Individual line parameters of CH_3OH ($J = 5–4$) are listed in Table 4. For NGC 1333-1 (IRAS 4B), and NGC 1333-2 (IRAS 2), 9 and 12 K-structure lines of CH_3OH were detected, respectively, as also reported in Maret et al. (2005). The CH_3OH ($J = 5–4$) lines detected in L1448-5, B1-1, and B1-3 accompany strong wing components. On the other hand, the CH_3OH ($J = 2–1$) lines (two or three K-structure) at 97 GHz were detected toward all the sources, whose line parameters are listed in Table 5.

The C_2H ($N = 3–2$) lines at 262 GHz were detected toward all the sources, as shown in Figure 3. These lines also trace a relatively dense and warm region as in the case of the CH_3OH line. Four hyperfine components were seen in all the sources. Their individual line parameters obtained with the Gaussian fit are listed in Table 9. The line parameters of the weakest

[10] For IC 348-3, the $C^{18}O$ integrated intensity did not meet the above criteria. Since the systemic velocity of the off-position is shifted by ∼1.5 km s^{-1} from the systemic velocity of IC 348-3, the influence on the analysis in this study would be negligible.

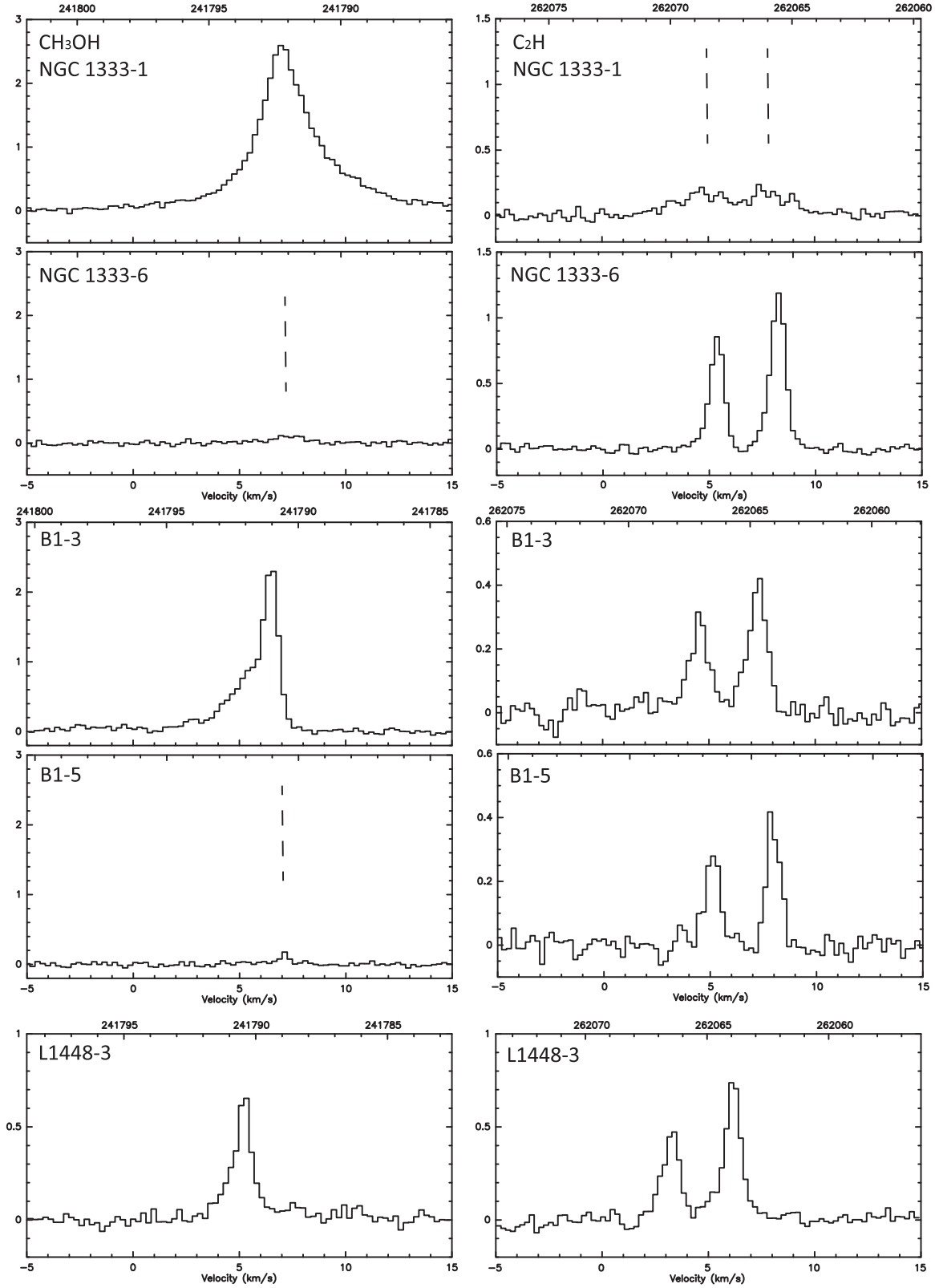

Figure 1. Line profiles of CH_3OH ($J = 5$–4, $K = 1$, E^-) and C_2H ($N = 3$–2, $J = 5/2$–$3/2$) observed with IRAM 30 m toward NGC 1333-1, NGC 1333-6, B1-3, B1-5, and L1448-3. Two hyperfine components, $F = 2$–1 (left) and $F = 3$–2 (right), are observed.

hyperfine component are missing for some sources, because the Gaussian fit was unsuccessful due to a poor S/N. For NGC 1333-1 and NGC 1333-16, the line shapes of the C_2H lines are quite different from those of the other sources; i.e., the intensities are weaker and the velocity widths are broader ($dv \sim 2.6\,\mathrm{km\,s^{-1}}$) than in the other sources. The C_2H emission toward NGC 1333-1 and NGC 1333-16 may be affected by the protostellar activities within the cores (e.g., molecular

Table 3
Physical Parameters

IDs	T_{rot} (K)	$N(CH_3OH)$ (10^{14} cm^{-2})	$N(C_2H)$ (10^{13} cm^{-2})	N(c-C_3H_2) (10^{12} cm^{-2})	$N(C_2H)/N(CH_3OH)$	N(c-C_3H_2)/$N(CH_3OH)$
NGC 1333-1	21 ± 2	5.2 ± 0.9	2.0 ± 0.3	4.5 ± 1.3	0.04 ± 0.01	0.009 ± 0.003
NGC 1333-2	19 ± 2	1.3 ± 0.4	4.1 ± 0.5	14 ± 3	0.32 ± 0.10	0.11 ± 0.04
NGC 1333-3	14 ± 1	1.2 ± 0.2	9.0 ± 1.1	5.4 ± 1.1	0.72 ± 0.11	0.04 ± 0.01
NGC 1333-4	12 ± 1	1.5 ± 0.2	4.1 ± 0.4	2.9 ± 1.0	0.27 ± 0.04	0.019 ± 0.007
NGC 1333-5	9 ± 1	1.9 ± 0.4	7.6 ± 0.8	6.0 ± 1.2	0.41 ± 0.06	0.032 ± 0.008
NGC 1333-6	9 ± 1	0.3 ± 0.1	11 ± 1	22 ± 3	3.9 ± 1.6	0.80 ± 0.34
NGC 1333-7	11 ± 1	3.0 ± 0.8	4.6 ± 0.7	6.0 ± 1.4	0.15 ± 0.03	0.020 ± 0.005
NGC 1333-8	10 ± 1	1.1 ± 0.4	7.1 ± 0.9	5.0 ± 1.4	0.66 ± 0.14	0.05 ± 0.02
NGC 1333-9	14 ± 3	0.2 ± 0.1	4.6 ± 1.2	<1.9	2.1 ± 1.2	0.09 ± 0.05
NGC 1333-10	13 ± 2	0.2 ± 0.07	0.9 ± 0.3	<1.9	0.50 ± 0.26	0.11 ± 0.05
NGC 1333-11	10 ± 1	0.9 ± 0.1	1.6 ± 0.3	2.1 ± 0.7	0.18 ± 0.04	0.024 ± 0.009
NGC 1333-12	10 ± 1	0.1 ± 0.04	0.8 ± 0.2	<1.5	0.72 ± 0.37	0.14 ± 0.06
NGC 1333-13	14 ± 2	0.3 ± 0.07	0.8 ± 0.2	<1.3	0.23 ± 0.07	0.039 ± 0.009
NGC 1333-14	11 ± 1	1.3 ± 0.1	1.7 ± 0.2	3.3 ± 0.8	0.14 ± 0.02	0.026 ± 0.007
NGC 1333-15	16 ± 2	0.8 ± 0.1	0.5 ± 0.2	<1.5	0.07 ± 0.03	0.020 ± 0.005
NGC 1333-16	21[a]	2.3 ± 0.5	1.8 ± 0.2	5.0 ± 0.6	0.08 ± 0.02	0.022 ± 0.005
NGC 1333-17	19[b]	0.5 ± 0.1	7.4 ± 0.6	8.9 ± 0.8	1.7 ± 0.3	0.20 ± 0.04
L1448-1	9 ± 1	1.4 ± 0.3	12 ± 1	31 ± 4	0.84 ± 0.18	0.23 ± 0.05
L1448-2	13 ± 1	2.9 ± 0.3	16 ± 2	24 ± 3	0.57 ± 0.08	0.09 ± 0.01
L1448-3	14 ± 1	0.8 ± 0.2	4.6 ± 0.6	12 ± 2	0.60 ± 0.14	0.15 ± 0.04
L1448-4	10 ± 1	1.9 ± 0.2	12 ± 1	10 ± 1	0.64 ± 0.09	0.05 ± 0.01
L1448-5	10 ± 1	2.1 ± 0.2	2.1 ± 0.4	7.4 ± 1.2	0.10 ± 0.02	0.034 ± 0.007
IC 348-1	11 ± 1	1.3 ± 0.2	5.0 ± 0.5	11 ± 2	0.38 ± 0.06	0.08 ± 0.02
IC 348-2	12 ± 1	0.6 ± 0.1	7.0 ± 0.7	12 ± 2	1.2 ± 0.23	0.21 ± 0.04
IC 348-3	10 ± 1	0.3 ± 0.1	3.2 ± 0.6	<1.6	0.96 ± 0.35	0.05 ± 0.02
IC 348-4	13 ± 1	0.6 ± 0.1	4.2 ± 0.5	6.7 ± 1.1	0.69 ± 0.13	0.11 ± 0.02
Barnard 5	10 ± 1	0.5 ± 0.1	9.0 ± 1.1	9.4 ± 1.9	1.9 ± 0.5	0.20 ± 0.06
B1-1	9 ± 1	0.8 ± 0.1	4.3 ± 0.5	14 ± 2	0.55 ± 0.12	0.18 ± 0.04
B1-2	9 ± 1	0.8 ± 0.1	7.3 ± 0.8	12 ± 2	0.96 ± 0.19	0.16 ± 0.03
B1-3	11 ± 1	4.2 ± 0.4	3.4 ± 0.4	5.9 ± 1.2	0.08 ± 0.01	0.014 ± 0.003
B1-4	9 ± 1	0.8 ± 0.2	8.3 ± 1.2	13 ± 2	1.1 ± 0.3	0.18 ± 0.05
B1-5	10 ± 1	0.4 ± 0.1	3.1 ± 0.5	5.2 ± 1.2	0.93 ± 0.34	0.16 ± 0.06
L1455-1	9 ± 1	<0.2	6.0 ± 1.1	7.7 ± 1.6	3.1 ± 1.5	0.39 ± 0.20
L1455-2	14 ± 1	0.7 ± 0.1	5.4 ± 0.7	9.0 ± 1.7	0.74 ± 0.15	0.12 ± 0.03
L1455-3	8 ± 1	0.3 ± 0.1	6.4 ± 0.9	5.1 ± 1.2	2.0 ± 0.7	0.16 ± 0.07
L1455-4	9 ± 1	0.5 ± 0.1	3.5 ± 0.6	1.8 ± 0.8	0.78 ± 0.26	0.04 ± 0.02
Reference						
L1527	8 ± 1	0.8 ± 0.1	33 ± 3	49 ± 3	4.1 ± 0.5	0.60 ± 0.07

Notes. Rotation temperatures are derived by the rotation diagram method from the CH_3OH (J = 2–1) and CH_3OH (J = 5–4) lines. Column densities are derived from the CH_3OH (J = 5–4, K = 1, E$^-$), C_2H (N = 3–2, J = 5/2–3/2, F = 3–2), and c-C_3H_2 ($3_{2,1}$–$2_{1,2}$) lines. Error bars are calculated for the rms noise and do not include calibration uncertainty (20%). As a reference, the column densities of L1527 are derived with the available IRAM 30 m/NRO 45 m data set.
[a] A rotation temperature of NGC 1333-1 is applied due to the lack of NRO data. The column density changes within 10% for the change in the assumed rotation temperature of ±5 K.
[b] A rotation temperature of NGC 1333-2 is applied due to the lack of NRO data. The column density changes within 10% for the change in the assumed rotation temperature of ±5 K.

outflows). For the other sources, the velocity widths of the C_2H emission mostly range from 0.6 to 1.5 km s^{-1}, indicating that the C_2H emission would mainly originate from protostellar envelopes or cavity walls of low-velocity outflows, rather than the main bodies of molecular outflows (e.g., Oya et al. 2014; Sakai et al. 2014a).

The c-C_3H_2 ($3_{2,1}$–$2_{1,2}$) line at 244 GHz was detected toward 30 sources, as shown in Figure 4. The line parameters obtained with the Gaussian fit are summarized in Table 7. For this line, the upper state energy is 18 K, and the critical density is 10^6 cm^{-3}. Hence, this line traces a moderately dense region. c-C_3H_2 is a carbon-chain related molecule, and traces the protostellar envelope as C_2H (Sakai et al. 2010, 2014b; Yoshida et al. 2015). The results show that the intensity of the $3_{2,1}$–$2_{1,2}$ line differs from source to source. The velocity widths of the c-C_3H_2 line are similar to those of C_2H. Therefore, the c-C_3H_2 and C_2H emission likely comes from almost the same region in each source.

3.2. Correlation of Integrated Intensities between C_2H and CH_3OH

A correlation plot between the integrated intensities of the C_2H (N = 3–2, J = 5/2–3/2, F = 3–2, E_u = 25 K) and CH_3OH (J = 5–4, K = 1, E$^-$, E_u = 40 K) lines is then prepared to understand how the intensity ratios differ among the observed sources. We employ the third weakest hyperfine

Table 4
Line Parameters of the CH_3OH ($J = 5$–4) Lines Observed with IRAM 30 m

IDs	Transition J, K	T_{MB}[a] (K)	dv[b] (km s^{-1})	$\int T_{MB} dv_{eff}$[c] (K km s^{-1})	$\int T_{MB} dv$[d] (K km s^{-1})	rms[e] (K)	V_{LSR} (km s^{-1})
NGC 1333-1	$J = 5$–4, $K = 2$ E$^-$	0.98	3.23 (0.49)	2.45 (0.33)	5.04 (0.49)	0.13	6.6
	$J = 5$–4, $K = 2$ A$^+$	0.22	2.53 (1.94)	0.54 (0.33)	0.85 (0.43)	0.13	6.2
	$J = 5$–4, $K = 1$ E$^+$	0.58	2.91 (0.81)	1.44 (0.33)	2.61 (0.47)	0.13	7.0
	$J = 5$–4, $K = 3$ E$^-$	0.08	3.66 (6.23)[f]	0.19 (0.33)[f]	0.38 (0.45)[f]	0.13	7.1
	$J = 5$–4, $K = 2$ A$^-$	0.27	4.40 (2.32)[f]	0.67 (0.33)[f]	1.65 (0.59)[f]	0.13	6.2
	$J = 5$–4, $K = 3$ A$^\pm$	0.34	3.98 (0.84)	0.87 (0.33)	2.18 (0.08)	0.13	5.8
	$J = 5$–4, $K = 0$ A$^+$	2.20	2.87 (0.10)	5.41 (0.33)	10.4 (0.08)	0.13	6.7
	$J = 5$–4, $K = 1$ E$^-$	1.94	2.82 (0.11)	4.84 (0.33)	8.56 (0.08)	0.13	6.8
	$J = 5$–4, $K = 0$ E$^+$	0.94	3.68 (0.31)	2.38 (0.33)	4.89 (0.08)	0.13	6.9
NGC 1333-2	$J = 5$–4, $K = 2$ E$^-$	0.49	3.05 (0.44)	0.67 (0.20)	2.24 (0.22)	0.15	6.5
	$J = 5$–4, $K = 2$ A$^+$	0.27	2.79 (0.70)	0.37 (0.20)	1.08 (0.21)	0.15	5.9
	$J = 5$–4, $K = 1$ E$^+$	0.34	2.95 (0.62)	0.47 (0.20)	1.47 (0.22)	0.15	6.8
	$J = 5$–4, $K = 3$ E$^-$	0.23	2.54 (0.65)	0.32 (0.20)	0.79 (0.19)	0.15	6.2
	$J = 5$–4, $K = 2$ A$^-$	0.30	3.51 (0.62)	0.42 (0.20)	1.47 (0.22)	0.15	5.6
	$J = 5$–4, $K = 3$ A$^\pm$	0.31	2.71 (0.62)	0.43 (0.20)	1.14 (0.23)	0.15	5.5
	$J = 5$–4, $K = 4$ E$^+$	0.18	2.02 (1.0)	0.25 (0.20)	0.60 (0.22)	0.15	6.1
	$J = 5$–4, $K = 4$ E$^-$	0.19	2.58 (0.79)	0.26 (0.20)	0.67 (0.17)	0.15	6.4
	$J = 5$–4, $K = 4$ A$^\pm$	0.22	2.48 (0.65)	0.30 (0.20)	0.75 (0.16)	0.15	6.0
	$J = 5$–4, $K = 0$ A$^+$	1.02	2.68 (0.22)	1.41 (0.20)	4.53 (0.20)	0.15	7.3
	$J = 5$–4, $K = 1$ E$^-$	0.84	3.05 (0.28)	1.17 (0.20)	4.08 (0.23)	0.15	7.4
	$J = 5$–4, $K = 0$ E$^+$	0.41	3.04 (0.53)	0.57 (0.20)	1.99 (0.21)	0.15	6.9
NGC 1333-3	$J = 5$–4, $K = 2$ E$^-$	0.16	0.92 (0.11)	0.16 (0.03)	0.18 (0.02)	0.03	7.3
	$J = 5$–4, $K = 0$ A$^+$	1.02	1.06 (0.02)	1.03 (0.03)	1.33 (0.02)	0.03	7.5
	$J = 5$–4, $K = 1$ E$^-$	0.84	0.98 (0.03)	0.84 (0.03)	1.07 (0.02)	0.03	7.7
	$J = 5$–4, $K = 0$ E$^+$	0.18	0.92 (0.13)	0.18 (0.03)	0.18 (0.02)	0.03	7.8
NGC 1333-4	$J = 5$–4, $K = 2$ E$^-$	0.14	0.63 (0.12)	0.15 (0.03)	0.14 (0.02)	0.03	7.9
	$J = 5$–4, $K = 0$ A$^+$	0.95	1.24 (0.02)	0.95 (0.03)	1.56 (0.02)	0.03	8.2
	$J = 5$–4, $K = 1$ E$^-$	0.81	1.17 (0.03)	0.82 (0.03)	1.25 (0.02)	0.03	8.4
	$J = 5$–4, $K = 0$ E$^+$	0.15	1.04 (0.18)	0.15 (0.03)	0.19 (0.02)	0.03	8.4
NGC 1333-5	$J = 5$–4, $K = 0$ A$^+$	0.68	0.76 (0.04)	0.67 (0.03)	0.69 (0.02)	0.03	7.5
	$J = 5$–4, $K = 1$ E$^-$	0.61	0.72 (0.04)	0.60 (0.03)	0.65 (0.02)	0.03	7.6
	$J = 5$–4, $K = 0$ E$^+$	0.14	0.62 (0.12)	0.14 (0.03)	0.21 (0.02)	0.03	7.6
NGC 1333-6	$J = 5$–4, $K = 0$ A$^+$	0.11	1.82 (0.31)	0.09 (0.02)	0.24 (0.03)	0.03	6.8
	$J = 5$–4, $K = 1$ E$^-$	0.10	2.27 (0.32)	0.09 (0.02)	0.23 (0.03)	0.03	7.2
	$J = 5$–4, $K = 0$ E$^+$	0.04	4.00 (1.08)	0.03 (0.02)	0.17 (0.04)	0.03	7.0
NGC 1333-7	$J = 5$–4, $K = 0$ A$^+$	1.13	1.24 (0.02)	1.75 (0.04)	1.86 (0.02)	0.03	7.3
	$J = 5$–4, $K = 1$ E$^-$	0.87	1.28 (0.03)	1.35 (0.04)	1.51 (0.02)	0.03	7.4
	$J = 5$–4, $K = 0$ E$^+$	0.11	1.52 (0.27)	0.17 (0.04)	0.22 (0.03)	0.03	7.3
NGC 1333-8	$J = 5$–4, $K = 0$ A$^+$	0.43	2.03 (0.07)	0.49 (0.03)	1.11 (0.03)	0.03	6.8
	$J = 5$–4, $K = 1$ E$^-$	0.33	2.04 (0.10)	0.38 (0.03)	0.89 (0.03)	0.03	6.9
	$J = 5$–4, $K = 0$ E$^+$	0.06	2.11 (0.42)	0.07 (0.03)	0.17 (0.03)	0.03	7.0
NGC 1333-9	$J = 5$–4, $K = 0$ A$^+$	0.08	1.00 (0.68)	0.08 (0.04)	0.16 (0.04)	0.03	7.2
	$J = 5$–4, $K = 1$ E$^-$	0.09	0.89 (0.16)	0.15 (0.04)	0.14 (0.02)	0.03	7.1
NGC 1333-10	$J = 5$–4, $K = 0$ A$^+$	0.07	1.87 (0.26)	0.09 (0.03)	0.12 (0.02)	0.02	7.3
	$J = 5$–4, $K = 1$ E$^-$	0.08	1.00 (0.18)	0.11 (0.03)	0.05 (0.01)	0.02	7.4
NGC 1333-11	$J = 5$–4, $K = 0$ A$^+$	0.67	1.08 (0.02)	0.40 (0.01)	0.92 (0.01)	0.02	8.2
	$J = 5$–4, $K = 1$ E$^-$	0.52	1.12 (0.03)	0.31 (0.01)	0.60 (0.02)	0.02	8.4
	$J = 5$–4, $K = 0$ E$^+$	0.07	1.43 (0.22)	0.04 (0.01)	0.09 (0.02)	0.03	8.3
NGC 1333-12	$J = 5$–4, $K = 0$ A$^+$	0.10	0.48 (0.10)	0.06 (0.01)	0.04 (0.01)	0.02	7.2
	$J = 5$–4, $K = 1$ E$^-$	0.07	0.77 (0.22)	0.04 (0.01)	0.07 (0.01)	0.02	7.4
NGC 1333-13	$J = 5$–4, $K = 0$ A$^+$	0.50	0.69 (0.03)	0.28 (0.01)	0.43 (0.01)	0.02	7.2
	$J = 5$–4, $K = 1$ E$^-$	0.43	0.69 (0.03)	0.24 (0.01)	0.43 (0.01)	0.02	7.3
NGC 1333-14	$J = 5$–4, $K = 2$ E$^-$	0.09	0.94 (0.18)	0.07 (0.02)	0.06 (0.02)	0.02	7.1
	$J = 5$–4, $K = 0$ A$^+$	0.91	1.17 (0.02)	0.80 (0.02)	1.27 (0.02)	0.02	7.6
	$J = 5$–4, $K = 1$ E$^-$	0.70	1.20 (0.02)	0.61 (0.02)	0.99 (0.02)	0.02	7.7
	$J = 5$–4, $K = 0$ E$^+$	0.12	1.17 (0.18)	0.10 (0.02)	0.18 (0.02)	0.02	7.8
NGC 1333-15	$J = 5$–4, $K = 0$ A$^+$	0.81	0.72 (0.02)	0.70 (0.02)	0.76 (0.01)	0.02	7.8
	$J = 5$–4, $K = 1$ E$^-$	0.67	0.68 (0.02)	0.58 (0.02)	0.61 (0.01)	0.02	8.0
	$J = 5$–4, $K = 0$ E$^+$	0.07	1.15(0.31)	0.06 (0.02)	0.11 (0.02)	0.02	8.0
NGC 1333-16	$J = 5$–4, $K = 2$ E$^-$	0.36	4.91 (1.96)	0.77 (0.36)	2.23 (0.52)	0.11	6.2
	$J = 5$–4, $K = 1$ E$^+$	0.21	4.72 (3.29)	0.45 (0.36)	1.17 (0.53)	0.11	6.7
	$J = 5$–4, $K = 2$ A$^-$	0.08	4.43 (7.02)[f]	0.16 (0.36)[f]	0.35 (0.46)[f]	0.11	6.3
	$J = 5$–4, $K = 3$ A$^\pm$	0.09	5.50 (6.57)[f]	0.20 (0.36)[f]	0.56 (0.50)[f]	0.11	6.1

Table 4
(Continued)

IDs	Transition J, K	T_{MB}[a] (K)	dv[b] (km s^{-1})	$\int T_{MB} dv_{eff}$[c] (K km s^{-1})	$\int T_{MB} dv$[d] (K km s^{-1})	rms[e] (K)	V_{LSR} (km s^{-1})
	$J = 5$–4, $K = 0$ A$^+$	1.21	4.88 (0.72)	2.57 (0.36)	8.44 (0.59)	0.11	6.4
	$J = 5$–4, $K = 1$ E$^-$	1.02	5.11 (0.78)	2.17 (0.36)	7.76 (0.71)	0.11	6.5
	$J = 5$–4, $K = 0$ E$^+$	0.37	5.01 (0.78)	0.79 (0.36)	2.31 (0.61)	0.11	6.5
NGC 1333-17	$J = 5$–4, $K = 2$ E$^-$	0.17	3.11 (0.39)	0.20 (0.05)	0.64 (0.22)	0.03	7.5
	$J = 5$–4, $K = 2$ A$^+$	0.11	3.62 (0.55)	0.13 (0.05)	0.46 (0.21)	0.03	7.0
	$J = 5$–4, $K = 1$ E$^+$	0.15	3.01 (0.39)	0.18 (0.05)	0.51 (0.22)	0.03	7.9
	$J = 5$–4, $K = 3$ E$^-$	0.10	3.43 (0.61)	0.12 (0.05)	0.41 (0.19)	0.03	7.5
	$J = 5$–4, $K = 2$ A$^-$	0.12	4.61 (0.57)	0.14 (0.05)	0.63 (0.22)	0.03	6.7
	$J = 5$–4, $K = 3$ A$^\pm$	0.12	6.00 (0.55)	0.14 (0.05)	0.78 (0.23)	0.03	8.1
	$J = 5$–4, $K = 4$ E$^+$	0.09	3.15 (0.50)	0.11 (0.05)	0.32 (0.17)	0.03	7.7
	$J = 5$–4, $K = 0$ A$^+$	0.41	1.29 (0.08)	0.48 (0.05)	0.71 (0.20)	0.03	7.8
	$J = 5$–4, $K = 1$ E$^-$	0.34	1.32 (0.10)	0.40 (0.05)	0.68 (0.23)	0.03	7.9
	$J = 5$–4, $K = 0$ E$^+$	0.16	2.84 (0.50)	0.19 (0.05)	0.61 (0.21)	0.03	7.8
L1448-1	$J = 5$–4, $K = 0$ A$^+$	0.28	1.08 (0.12)	0.43 (0.05)	0.35 (0.01)	0.03	4.1
	$J = 5$–4, $K = 1$ E$^-$	0.25	1.17 (0.11)	0.38 (0.05)	0.34 (0.01)	0.03	4.3
	$J = 5$–4, $K = 0$ E$^+$	0.12	0.30 (0.10)	0.19 (0.05)	0.08 (0.01)	0.03	4.5
L1448-2	$J = 5$–4, $K = 2$ E$^-$	0.24	1.46 (0.15)	0.45 (0.05)	0.44 (0.02)	0.03	4.2
	$J = 5$–4, $K = 1$ E$^+$	0.16	1.14 (0.16)	0.30 (0.05)	0.29 (0.02)	0.03	4.7
	$J = 5$–4, $K = 0$ A$^+$	1.15	1.28 (0.03)	2.16 (0.05)	2.22 (0.03)	0.03	4.2
	$J = 5$–4, $K = 1$ E$^-$	0.94	1.21 (0.03)	1.76 (0.05)	1.46 (0.02)	0.03	4.3
	$J = 5$–4, $K = 0$ E$^+$	0.34	1.33 (0.09)	0.63 (0.05)	0.54 (0.03)	0.03	4.5
L1448-3	$J = 5$–4, $K = 2$ E$^-$	0.16	2.65 (0.48)	0.17 (0.05)	0.67 (0.06)	0.05	4.6
	$J = 5$–4, $K = 1$ E$^+$	0.13	1.30 (0.36)	0.14 (0.05)	0.27 (0.04)	0.05	5.0
	$J = 5$–4, $K = 0$ A$^+$	0.58	1.18 (0.09)	0.63 (0.05)	1.04 (0.04)	0.05	4.6
	$J = 5$–4, $K = 1$ E$^-$	0.48	1.14 (0.11)	0.52 (0.05)	0.99 (0.04)	0.05	4.8
	$J = 5$–4, $K = 0$ E$^+$	0.24	1.16 (0.26)	0.26 (0.05)	0.56 (0.05)	0.05	4.9
L1448-4	$J = 5$–4, $K = 2$ E$^-$	0.10	1.21 (0.33)	0.10 (0.03)	0.21 (0.03)	0.03	3.3
	$J = 5$–4, $K = 0$ A$^+$	0.82	0.72 (0.03)	0.82 (0.03)	0.78 (0.02)	0.03	3.7
	$J = 5$–4, $K = 1$ E$^-$	0.71	0.68 (0.03)	0.71 (0.03)	0.69 (0.02)	0.03	3.9
	$J = 5$–4, $K = 0$ E$^+$	0.09	1.38 (0.69)	0.09 (0.03)	0.13 (0.04)	0.03	3.8
L1448-5	$J = 5$–4, $K = 2$ E$^-$	0.06	3.27 (0.91)	0.05 (0.03)	0.19 (0.03)	0.04	3.6
	$J = 5$–4, $K = 1$ E$^+$	0.12	0.56 (0.25)	0.08 (0.03)	0.04 (0.03)	0.04	4.1
	$J = 5$–4, $K = 0$ A$^+$	1.32	0.97 (0.03)	0.87 (0.03)	2.37 (0.03)	0.04	3.8
	$J = 5$–4, $K = 1$ E$^-$	1.20	0.86 (0.03)	0.80 (0.03)	1.89 (0.03)	0.04	3.9
	$J = 5$–4, $K = 0$ E$^+$	0.27	0.60 (0.13)	0.18 (0.03)	0.27 (0.03)	0.04	3.9
IC 348-1	$J = 5$–4, $K = 2$ E$^-$	0.07	0.96 (0.40)	0.07 (0.03)	0.09 (0.02)	0.03	8.3
	$J = 5$–4, $K = 0$ A$^+$	0.93	0.63 (0.02)	0.81 (0.03)	0.81 (0.02)	0.03	8.6
	$J = 5$–4, $K = 1$ E$^-$	0.76	0.62 (0.03)	0.65 (0.03)	0.74 (0.02)	0.03	8.7
	$J = 5$–4, $K = 0$ E$^+$	0.13	1.04 (0.17)	0.10 (0.03)	0.13 (0.02)	0.03	8.8
IC 348-2	$J = 5$–4, $K = 2$ E$^-$	0.07	1.59 (0.29)	0.07 (0.03)	0.12 (0.02)	0.03	8.2
	$J = 5$–4, $K = 0$ A$^+$	0.36	0.80 (0.06)	0.40 (0.03)	0.37 (0.02)	0.02	8.4
	$J = 5$–4, $K = 1$ E$^-$	0.28	0.74 (0.07)	0.31 (0.03)	0.32 (0.02)	0.02	8.5
	$J = 5$–4, $K = 0$ E$^+$	0.06	1.29 (0.47)	0.07 (0.03)	0.10 (0.02)	0.03	8.5
IC 348-3	$J = 5$–4, $K = 0$ A$^+$	0.16	1.16 (0.10)	0.18 (0.03)	0.15 (0.02)	0.02	9.9
	$J = 5$–4, $K = 1$ E$^-$	0.11	1.38 (0.16)	0.13 (0.03)	0.17 (0.02)	0.02	10
IC 348-4	$J = 5$–4, $K = 2$ E$^-$	0.09	0.36 (0.11)	0.08 (0.02)	0.06 (0.01)	0.02	7.6
	$J = 5$–4, $K = 0$ A$^+$	0.46	0.76 (0.04)	0.40 (0.02)	0.52 (0.01)	0.02	8.0
	$J = 5$–4, $K = 1$ E$^-$	0.41	0.69 (0.04)	0.36 (0.02)	0.46 (0.02)	0.02	8.2
Barnard 5	$J = 5$–4, $K = 0$ A$^+$	0.26	0.80 (0.07)	0.22 (0.02)	0.26 (0.02)	0.02	9.6
	$J = 5$–4, $K = 1$ E$^-$	0.19	0.80 (0.08)	0.16 (0.02)	0.18 (0.02)	0.02	9.8
B1-1	$J = 5$–4, $K = 2$ E$^-$	0.07	4.64 (0.24)	0.07 (0.03)	0.46 (0.09)	0.02	7.0
	$J = 5$–4, $K = 1$ E$^+$	0.05	3.33(0.24)	0.06 (0.03)	0.20 (0.03)	0.02	6.5
	$J = 5$–4, $K = 0$ A$^+$	0.25	4.52 (0.24)	0.39 (0.03)	1.75 (0.07)	0.02	6.2
	$J = 5$–4, $K = 1$ E$^-$	0.21	4.54 (0.24)	0.23 (0.03)	1.47 (0.11)	0.02	6.9
	$J = 5$–4, $K = 0$ E$^+$	0.08	2.66 (0.24)	0.08 (0.03)	0.21 (0.04)	0.02	6.5
B1-2	$J = 5$–4, $K = 0$ A$^+$	0.42	0.66 (0.04)	0.29 (0.02)	0.33 (0.01)	0.02	6.2
	$J = 5$–4, $K = 1$ E$^-$	0.30	0.68 (0.05)	0.20 (0.02)	0.27 (0.01)	0.02	6.1
B1-3	$J = 5$–4, $K = 2$ E$^-$	0.18	1.99 (0.22)	0.22 (0.05)	0.40 (0.04)	0.04	5.2
	$J = 5$–4, $K = 1$ E$^+$	0.10	1.89 (0.36)	0.12 (0.05)	0.20 (0.04)	0.04	5.7
	$J = 5$–4, $K = 0$ A$^+$	1.96	1.45 (0.07)	2.50 (0.05)	3.99 (0.04)	0.04	5.8
	$J = 5$–4, $K = 1$ E$^-$	1.65	1.37 (0.03)	2.10 (0.05)	3.16 (0.03)	0.04	5.9
	$J = 5$–4, $K = 0$ E$^+$	0.26	2.31 (0.18)	0.33 (0.05)	0.66 (0.04)	0.04	5.6
B1-4	$J = 5$–4, $K = 0$ A$^+$	0.29	0.78 (0.10)	0.31 (0.03)	0.33 (0.02)	0.03	6.5

Table 4
(Continued)

IDs	Transition J, K	T_{MB}[a] (K)	dv[b] (km s^{-1})	$\int T_{MB} dv_{eff}$[c] (K km s^{-1})	$\int T_{MB} dv$[d] (K km s^{-1})	rms[e] (K)	V_{LSR} (km s^{-1})
	$J = 5$–4, $K = 1$ E$^-$	0.21	0.71 (0.09)	0.22 (0.03)	0.18 (0.02)	0.03	6.5
B1-5	$J = 5$–4, $K = 0$ A$^+$	0.17	0.49 (0.11)	0.16 (0.02)	0.16 (0.02)	0.03	5.6
	$J = 5$–4, $K = 1$ E$^-$	0.12	0.82 (0.21)	0.11 (0.02)	0.11 (0.01)	0.03	6.6
L1455-1	...	...	...	0.05 (0.02)	0.06	0.02	...
L1455-2	$J = 5$–4, $K = 2$ E$^-$	0.09	4.65 (0.66)	0.11 (0.03)	0.59 (0.04)	0.03	4.1
	$J = 5$–4, $K = 0$ A$^+$	0.47	1.38 (0.07)	0.57 (0.03)	0.89 (0.02)	0.03	4.4
	$J = 5$–4, $K = 1$ E$^-$	0.40	1.26 (0.07)	0.49 (0.03)	0.92 (0.02)	0.03	4.6
	$J = 5$–4, $K = 0$ E$^+$	0.07	5.97 (0.85)	0.08 (0.03)	0.44 (0.04)	0.03	4.1
L1455-3	$J = 5$–4, $K = 0$ A$^+$	0.20	0.87 (0.09)	0.16 (0.02)	0.18 (0.02)	0.02	4.4
	$J = 5$–4, $K = 1$ E$^-$	0.10	1.69 (0.23)	0.08 (0.02)	0.15 (0.02)	0.02	4.7
L1455-4	$J = 5$–4, $K = 0$ A$^+$	0.14	1.06 (0.13)	0.16 (0.02)	0.16 (0.02)	0.02	4.7
	$J = 5$–4, $K = 1$ E$^-$	0.12	0.78 (0.15)	0.14 (0.02)	0.12 (0.02)	0.02	4.8

Notes. The errors are 1σ. The upper limit to the integrated intensity is calculated as $\int T_{MB} dv < 3\sigma \times \sqrt{(dv/dv_{res})}\ dv_{res}$, where dv is the assumed line width (0.8 km s^{-1}) and dv_{res} is the velocity resolution per channel.
[a] Obtained by the Gaussian fit.
[b] The wing components are excluded in the Gaussian fit.
[c] Derived using the C_2H velocity width.
[d] The wing components are included when calculating the integrated intensity.
[e] The rms noise averaged over the line width.
[f] The error in the Gaussian fitting is large.

Table 5
Line Parameters of the CH_3OH ($J = 2$–1) Lines Observed with the Nobeyama 45 m Telescope

IDs	Transition J, K	T_{MB}[a] (K)	dv[b] (km s^{-1})	$\int T_{MB} dv_{eff}$[c] (K km s^{-1})	$\int T_{MB} dv$[d] (K km s^{-1})	rms[e] (K)	V_{LSR} (km s^{-1})
NGC 1333-1	$J = 2$–1, $K = 1$ E$^-$	1.40	2.16 (0.04)	3.50 (0.04)	3.53 (0.04)	0.02	7.7
	$J = 2$–1, $K = 0$ A$^+$	1.97	2.15 (0.04)	4.92 (0.04)	5.94 (0.04)	0.02	7.5
	$J = 2$–1, $K = 0$ E$^+$	0.47	2.56 (0.04)	1.18 (0.04)	1.73 (0.04)	0.02	6.8
NGC 1333-2	$J = 2$–1, $K = 1$ E$^-$	1.38	1.32 (0.02)	1.91 (0.02)	2.57 (0.02)	0.02	7.7
	$J = 2$–1, $K = 0$ A$^+$	1.73	1.37 (0.02)	2.39 (0.02)	3.32 (0.02)	0.02	7.9
	$J = 2$–1, $K = 0$ E$^+$	0.27	1.56 (0.02)	0.38 (0.02)	0.62 (0.02)	0.02	7.6
NGC 1333-3	$J = 2$–1, $K = 1$ E$^-$	0.82	1.21 (0.02)	0.82 (0.02)	1.15 (0.02)	0.02	7.8
	$J = 2$–1, $K = 0$ A$^+$	1.27	1.14 (0.02)	1.27 (0.02)	1.69 (0.02)	0.02	7.9
	$J = 2$–1, $K = 0$ E$^+$	0.22	1.13 (0.02)	0.22 (0.02)	0.23 (0.02)	0.02	7.9
NGC 1333-4	$J = 2$–1, $K = 1$ E$^-$	1.18	1.19 (0.02)	1.19 (0.02)	1.68 (0.02)	0.02	8.5
	$J = 2$–1, $K = 0$ A$^+$	1.74	1.18 (0.02)	1.76 (0.02)	2.52 (0.02)	0.02	8.6
	$J = 2$–1, $K = 0$ E$^+$	0.35	1.01 (0.02)	0.35 (0.02)	0.42 (0.02)	0.02	8.7
NGC 1333-5	$J = 2$–1, $K = 1$ E$^-$	1.54	0.98 (0.01)	1.52 (0.01)	1.83 (0.01)	0.01	7.7
	$J = 2$–1, $K = 0$ A$^+$	2.03	1.04(0.02)	2.00 (0.01)	2.45 (0.02)	0.01	7.9
	$J = 2$–1, $K = 0$ E$^+$	0.32	0.92 (0.01)	0.31 (0.01)	0.38 (0.01)	0.01	7.9
NGC 1333-6	$J = 2$–1, $K = 1$ E$^-$	0.23	1.17 (0.02)	0.21 (0.01)	0.32 (0.02)	0.02	7.4
	$J = 2$–1, $K = 0$ A$^+$	0.29	1.02 (0.02)	0.26 (0.01)	0.39 (0.02)	0.02	7.2
NGC 1333-7	$J = 2$–1, $K = 1$ E$^-$	2.01	1.34 (0.02)	3.11 (0.02)	3.03 (0.02)	0.02	7.7
	$J = 2$–1, $K = 0$ A$^+$	2.64	1.42 (0.02)	4.08 (0.02)	4.31 (0.02)	0.02	7.5
	$J = 2$–1, $K = 0$ E$^+$	0.38	1.32 (0.02)	0.58 (0.02)	0.58 (0.02)	0.02	7.6
NGC 1333-8	$J = 2$–1, $K = 1$ E$^-$	1.02	1.61 (0.02)	1.17 (0.02)	1.89 (0.02)	0.02	7.4
	$J = 2$–1, $K = 0$ A$^+$	1.45	1.54 (0.02)	1.68 (0.02)	2.54 (0.02)	0.02	7.5
	$J = 2$–1, $K = 0$ E$^+$	0.15	1.78 (0.03)	0.17 (0.02)	0.31 (0.03)	0.02	7.6
NGC 1333-9	$J = 2$–1, $K = 1$ E$^-$	0.09	1.98 (0.03)	0.14 (0.03)	0.18 (0.03)	0.02	8.1
	$J = 2$–1, $K = 0$ A$^+$	0.11	1.92 (0.03)	0.18 (0.03)	0.19 (0.03)	0.02	7.2
NGC 1333-10	$J = 2$–1, $K = 1$ E$^-$	0.09	1.91 (0.03)	0.12 (0.02)	0.20 (0.03)	0.02	8.1
	$J = 2$–1, $K = 0$ A$^+$	0.12	2.36 (0.04)	0.16 (0.02)	0.25 (0.04)	0.02	7.9
NGC 1333-11	$J = 2$–1, $K = 1$ E$^-$	1.41	1.21 (0.02)	0.85 (0.01)	1.90 (0.02)	0.01	8.5
	$J = 2$–1, $K = 0$ A$^+$	1.84	1.24 (0.02)	1.12 (0.01)	2.64 (0.02)	0.01	8.6
	$J = 2$–1, $K = 0$ E$^+$	0.33	1.14 (0.02)	0.20 (0.01)	0.43 (0.02)	0.01	8.7
NGC 1333-12	$J = 2$–1, $K = 1$ E$^-$	0.15	0.86 (0.01)	0.08 (0.01)	0.17 (0.01)	0.03	7.8
	$J = 2$–1, $K = 0$ A$^+$	0.20	1.02 (0.02)	0.12 (0.01)	0.29 (0.02)	0.03	7.5
NGC 1333-13	$J = 2$–1, $K = 1$ E$^-$	0.39	0.96 (0.02)	0.22 (0.01)	0.41 (0.01)	0.02	7.7
	$J = 2$–1, $K = 0$ A$^+$	0.62	0.95 (0.02)	0.35 (0.01)	0.59 (0.01)	0.02	7.5

Table 5
(Continued)

IDs	Transition J, K	T_{MB}[a] (K)	dv[b] (km s^{-1})	$\int T_{MB} dv_{eff}$[c] (K km s^{-1})	$\int T_{MB} dv$[d] (K km s^{-1})	rms[e] (K)	V_{LSR} (km s^{-1})
NGC 1333-14	$J = 2–1$, $K = 1$ E$^-$	1.08	1.32 (0.02)	0.95 (0.01)	1.57 (0.02)	0.02	7.7
	$J = 2–1$, $K = 0$ A$^+$	1.57	1.32 (0.02)	1.38 (0.01)	2.31 (0.02)	0.02	7.9
	$J = 2–1$, $K = 0$ E$^+$	0.24	1.65 (0.03)	0.21 (0.01)	0.40 (0.02)	0.02	7.9
NGC 1333-15	$J = 2–1$, $K = 1$ E$^-$	0.24	0.95 (0.02)	0.21 (0.01)	0.24 (0.01)	0.02	7.4
	$J = 2–1$, $K = 0$ A$^+$	0.30	1.03 (0.02)	0.26 (0.01)	0.35 (0.02)	0.02	7.5
L1448-1	$J = 2–1$, $K = 1$ E$^-$	0.93	1.17 (0.02)	1.45 (0.03)	1.28 (0.02)	0.02	4.5
	$J = 2–1$, $K = 0$ A$^+$	1.22	1.18 (0.02)	1.96 (0.03)	1.80 (0.02)	0.02	4.6
	$J = 2–1$, $K = 0$ E$^+$	0.23	1.14 (0.02)	0.35 (0.03)	0.39 (0.02)	0.02	4.7
L1448-2	$J = 2–1$, $K = 1$ E$^-$	1.34	1.03 (0.02)	2.52 (0.03)	1.74 (0.02)	0.02	4.5
	$J = 2–1$, $K = 0$ A$^+$	1.73	1.09 (0.02)	3.26 (0.03)	2.99 (0.02)	0.02	4.3
	$J = 2–1$, $K = 0$ E$^+$	0.39	1.56 (0.03)	0.74 (0.03)	1.32 (0.03)	0.02	4.7
L1448-3	$J = 2–1$, $K = 1$ E$^-$	0.64	1.77 (0.03)	0.69 (0.02)	2.58 (0.03)	0.02	4.8
	$J = 2–1$, $K = 0$ A$^+$	0.74	1.71 (0.03)	0.80 (0.02)	1.70 (0.03)	0.02	5.0
	$J = 2–1$, $K = 0$ E$^+$	0.08	1.30 (0.02)	0.09 (0.02)	0.11 (0.02)	0.02	5.0
L1448-4	$J = 2–1$, $K = 1$ E$^-$	1.92	0.81 (0.01)	1.91 (0.02)	1.74 (0.01)	0.02	4.1
	$J = 2–1$, $K = 0$ A$^+$	2.39	0.87 (0.01)	2.38 (0.02)	2.34 (0.01)	0.02	4.3
	$J = 2–1$, $K = 0$ E$^+$	0.35	0.84 (0.01)	0.35 (0.02)	0.34 (0.01)	0.02	4.3
L1448-5	$J = 2–1$, $K = 1$ E$^-$	2.31	1.05 (0.02)	1.57 (0.01)	5.19 (0.02)	0.02	4.1
	$J = 2–1$, $K = 0$ A$^+$	2.65	1.10 (0.02)	1.80 (0.01)	6.27 (0.02)	0.02	4.3
	$J = 2–1$, $K = 0$ E$^+$	0.49	0.92 (0.02)	0.33 (0.01)	1.12 (0.02)	0.02	4.3
IC 348-1	$J = 2–1$, $K = 1$ E$^-$	0.93	1.25 (0.02)	0.80 (0.01)	1.21 (0.02)	0.02	9.1
	$J = 2–1$, $K = 0$ A$^+$	1.31	1.24 (0.02)	1.13 (0.01)	1.81 (0.02)	0.02	9.3
	$J = 2–1$, $K = 0$ E$^+$	0.25	1.14 (0.02)	0.22 (0.01)	0.40 (0.02)	0.02	9.3
IC 348-2	$J = 2–1$, $K = 1$ E$^-$	0.49	0.90 (0.01)	0.53 (0.02)	0.49 (0.01)	0.02	8.8
	$J = 2–1$, $K = 0$ A$^+$	0.69	0.89 (0.01)	0.76 (0.02)	0.77 (0.01)	0.02	8.5
	$J = 2–1$, $K = 0$ E$^+$	0.13	0.98 (0.02)	0.15 (0.02)	0.16 (0.01)	0.02	8.9
IC 348-3	$J = 2–1$, $K = 1$ E$^-$	0.24	1.48 (0.02)	0.26 (0.02)	0.40 (0.05)	0.02	10
	$J = 2–1$, $K = 0$ A$^+$	0.31	1.59 (0.02)	0.35 (0.02)	0.57 (0.05)	0.02	10
IC 348-4	$J = 2–1$, $K = 1$ E$^-$	0.72	0.88 (0.01)	0.64 (0.01)	0.76 (0.01)	0.02	8.4
	$J = 2–1$, $K = 0$ A$^+$	1.11	0.84 (0.01)	0.98 (0.01)	1.07 (0.01)	0.02	8.5
	$J = 2–1$, $K = 0$ E$^+$	0.20	0.83 (0.01)	0.18 (0.01)	0.20 (0.01)	0.02	8.6
Barnard 5	$J = 2–1$, $K = 1$ E$^-$	0.43	1.00 (0.02)	0.36 (0.01)	0.43 (0.02)	0.02	9.9
	$J = 2–1$, $K = 0$ A$^+$	0.60	1.02 (0.02)	0.51 (0.01)	0.63 (0.02)	0.02	9.7
B1-1	$J = 2–1$, $K = 1$ E$^-$	1.16	1.35 (0.02)	1.25 (0.02)	1.94 (0.02)	0.02	6.5
	$J = 2–1$, $K = 0$ A$^+$	1.60	1.27 (0.02)	1.72 (0.02)	2.44 (0.02)	0.02	6.3
	$J = 2–1$, $K = 0$ E$^+$	0.18	1.33 (0.02)	0.19 (0.02)	0.25 (0.02)	0.02	6.3
B1-2	$J = 2–1$, $K = 1$ E$^-$	1.33	0.86 (0.01)	0.90 (0.01)	1.25 (0.01)	0.02	6.5
	$J = 2–1$, $K = 0$ A$^+$	1.62	0.93 (0.02)	1.10 (0.01)	1.64 (0.01)	0.02	6.7
	$J = 2–1$, $K = 0$ E$^+$	0.18	0.89 (0.01)	0.12 (0.01)	0.15 (0.01)	0.02	6.7
B1-3	$J = 2–1$, $K = 1$ E$^-$	2.24	1.16 (0.02)	2.86 (0.02)	3.23 (0.02)	0.02	6.5
	$J = 2–1$, $K = 0$ A$^+$	2.97	1.19 (0.02)	3.80 (0.02)	4.47 (0.02)	0.02	6.3
	$J = 2–1$, $K = 0$ E$^+$	0.45	1.22 (0.02)	0.58 (0.02)	0.66 (0.02)	0.02	6.3
B1-4	$J = 2–1$, $K = 1$ E$^-$	0.66	0.90 (0.01)	0.72 (0.02)	0.63 (0.01)	0.02	7.2
	$J = 2–1$, $K = 0$ A$^+$	0.98	0.88 (0.01)	1.06 (0.02)	0.86 (0.01)	0.02	7.0
	$J = 2–1$, $K = 0$ E$^+$	0.10	0.80 (0.01)	0.11 (0.02)	0.09 (0.01)	0.02	7.1
B1-5	$J = 2–1$, $K = 1$ E$^-$	0.29	0.92 (0.02)	0.27 (0.01)	0.34 (0.01)	0.02	7.2
	$J = 2–1$, $K = 0$ A$^+$	0.40	1.10 (0.02)	0.37 (0.01)	0.53 (0.02)	0.02	7.0
L1455-1	$J = 2–1$, $K = 1$ E$^-$	0.19	0.61 (0.01)	0.16 (0.01)	0.11 (0.01)	0.02	5.2[f]
	$J = 2–1$, $K = 0$ A$^+$	0.22	0.79 (0.01)	0.18 (0.01)	0.17 (0.01)	0.02	5.4[f]
L1455-2	$J = 2–1$, $K = 1$ E$^-$	0.34	1.24 (0.02)	0.41 (0.02)	0.55 (0.02)	0.02	4.8[f]
	$J = 2–1$, $K = 0$ A$^+$	0.49	1.27 (0.02)	0.59 (0.02)	0.87 (0.02)	0.02	5.0[f]
L1455-3	$J = 2–1$, $K = 1$ E$^-$	0.33	1.67 (0.03)	0.26 (0.01)	0.54 (0.03)	0.02	5.6[f]
	$J = 2–1$, $K = 0$ A$^+$	0.49	1.65 (0.03)	0.40 (0.01)	0.78(0.02)	0.02	5.8[f]
L1455-4	$J = 2–1$, $K = 1$ E$^-$	0.33	1.46 (0.02)	0.36 (0.02)	0.61 (0.02)	0.02	5.2[f]
	$J = 2–1$, $K = 0$ A$^+$	0.45	1.41 (0.02)	0.50 (0.02)	0.88 (0.02)	0.02	5.0[f]

Notes.
[a] Obtained by the Gaussian fit.
[b] The wing components are excluded in the Gaussian fit.
[c] Derived using the C_2H velocity widths.
[d] The wing components are included when calculating the integrated intensity.
[e] The rms noise averaged over the line width.
[f] Only for the L1455 region, V_{LSR} is corrected by 9 km s^{-1} due to a problem with the NRO 45 m. It is recovered using the V_{LSR} obtained by IRAM 30 m.

Table 6
Line Parameters of the C_2H ($N = 3$–2) Lines Observed with IRAM 30 m

IDs	Transition J, F	T_{MB}[a] (K)	dv (km s^{-1})	$\int T_{MB} dv$ (K km s^{-1})	rms[b] (K)	V_{LSR} (km s^{-1})
NGC 1333-1	$J = 5/2$–$3/2$, $F = 2$–1	0.16	2.62 (0.20)	0.45 (0.02)	0.03	6.4
	$J = 5/2$–$3/2$, $F = 3$–2	0.16	2.27 (0.20)	0.39 (0.02)	0.03	6.9
	$J = 7/2$–$5/2$, $F = 3$–2	0.22	2.43 (0.20)	0.57 (0.02)	0.03	6.6
	$J = 7/2$–$5/2$, $F = 4$–3	0.27	2.10 (0.20)	0.60 (0.02)	0.03	6.9
NGC 1333-2	$J = 5/2$–$3/2$, $F = 2$–1	0.42	1.30 (0.07)	0.58 (0.02)	0.03	7.6
	$J = 5/2$–$3/2$, $F = 3$–2	0.60	1.19 (0.04)	0.76 (0.02)	0.03	7.6
	$J = 7/2$–$5/2$, $F = 3$–2	0.61	1.26 (0.05)	0.83 (0.02)	0.03	7.5
	$J = 7/2$–$5/2$, $F = 4$–3	0.72	1.45 (0.04)	1.10 (0.03)	0.03	7.5
NGC 1333-3	$J = 5/2$–$3/2$, $F = 2$–1	0.99	0.91 (0.22)	0.96 (0.05)	0.03	8.2
	$J = 5/2$–$3/2$, $F = 3$–2	1.37	0.97 (0.22)	1.41 (0.05)	0.03	8.2
	$J = 7/2$–$5/2$, $F = 3$–2	1.46	0.94 (0.22)	1.46 (0.05)	0.03	8.2
	$J = 7/2$–$5/2$, $F = 4$–3	1.83	0.95 (0.22)	1.85 (0.05)	0.03	8.1
NGC 1333-4	$J = 5/2$–$3/2$, $F = 2$–1	0.36	0.92 (0.06)	0.36 (0.02)	0.03	8.7
	$J = 5/2$–$3/2$, $F = 3$–2	0.62	0.85 (0.03)	0.56 (0.02)	0.03	8.7
	$J = 7/2$–$5/2$, $F = 3$–2	0.65	0.97 (0.03)	0.67 (0.02)	0.03	8.6
	$J = 7/2$–$5/2$, $F = 4$–3	0.76	1.05 (0.03)	0.85 (0.02)	0.03	8.6
NGC 1333-5	$J = 5/2$–$3/2$, $F = 2$–1	0.56	0.94 (0.04)	0.56 (0.02)	0.03	7.7
	$J = 5/2$–$3/2$, $F = 3$–2	0.78	0.90 (0.03)	0.75 (0.02)	0.03	7.7
	$J = 7/2$–$5/2$, $F = 3$–2	0.74	0.94 (0.03)	0.74 (0.02)	0.03	7.7
	$J = 7/2$–$5/2$, $F = 4$–3	0.97	0.93 (0.02)	0.95 (0.02)	0.03	7.6
NGC 1333-6	$J = 5/2$–$3/2$, $F = 2$–1	0.85	0.80 (0.02)	0.72 (0.02)	0.02	7.2
	$J = 5/2$–$3/2$, $F = 3$–2	1.17	0.85 (0.02)	1.05 (0.02)	0.02	7.3
	$J = 7/2$–$5/2$, $F = 3$–2	1.21	0.85 (0.02)	1.09 (0.02)	0.02	7.2
	$J = 7/2$–$5/2$, $F = 4$–3	1.53	0.86 (0.01)	1.39 (0.02)	0.02	7.2
NGC 1333-7	$J = 5/2$–$3/2$, $F = 2$–1	0.26	1.76 (0.22)	0.49 (0.02)	0.02	8.0
	$J = 5/2$–$3/2$, $F = 3$–2	0.40	1.33 (0.22)	0.56 (0.02)	0.02	8.0
	$J = 7/2$–$5/2$, $F = 3$–2	0.44	1.46 (0.22)	0.68 (0.02)	0.02	8.0
	$J = 7/2$–$5/2$, $F = 4$–3	0.58	1.27 (0.22)	0.78 (0.02)	0.02	7.9
NGC 1333-8	$J = 5/2$–$3/2$, $F = 2$–1	0.44	1.06 (0.04)	0.49 (0.02)	0.02	6.6
	$J = 5/2$–$3/2$, $F = 3$–2	0.64	1.09 (0.03)	0.75 (0.02)	0.02	6.6
	$J = 7/2$–$5/2$, $F = 3$–2	0.66	1.06 (0.03)	0.75 (0.02)	0.02	6.6
	$J = 7/2$–$5/2$, $F = 4$–3	0.89	1.12 (0.02)	1.06 (0.02)	0.02	6.6
NGC 1333-9	$J = 5/2$–$3/2$, $F = 2$–1	0.33	1.54 (0.07)	0.54 (0.02)	0.02	7.6
	$J = 5/2$–$3/2$, $F = 3$–2	0.47	1.45 (0.05)	0.72 (0.02)	0.02	7.6
	$J = 7/2$–$5/2$, $F = 3$–2	0.51	1.58 (0.06)	0.86 (0.02)	0.02	7.6
	$J = 7/2$–$5/2$, $F = 4$–3	0.65	1.47 (0.04)	1.01 (0.02)	0.02	7.5
NGC 1333-10	$J = 5/2$–$3/2$, $F = 3$–2	0.10	1.25 (0.18)	0.13 (0.02)	0.02	7.6
	$J = 7/2$–$5/2$, $F = 3$–2	0.12	1.09 (0.18)	0.14 (0.02)	0.02	7.5
	$J = 7/2$–$5/2$, $F = 4$–3	0.13	1.49 (0.24)	0.21 (0.02)	0.02	7.3
NGC 1333-11	$J = 5/2$–$3/2$, $F = 2$–1	0.18	0.63 (0.09)	0.12 (0.01)	0.02	8.5
	$J = 5/2$–$3/2$, $F = 3$–2	0.27	0.58 (0.06)	0.17 (0.01)	0.02	8.5
	$J = 7/2$–$5/2$, $F = 3$–2	0.25	0.56 (0.07)	0.15 (0.01)	0.02	8.5
	$J = 7/2$–$5/2$, $F = 4$–3	0.31	0.50 (0.05)	0.17 (0.01)	0.02	8.5
NGC 1333-12	$J = 5/2$–$3/2$, $F = 2$–1	0.12	0.47 (0.14)	0.06 (0.01)	0.02	7.5
	$J = 5/2$–$3/2$, $F = 3$–2	0.14	0.55 (0.11)	0.08 (0.01)	0.02	7.6
	$J = 7/2$–$5/2$, $F = 3$–2	0.16	0.63 (0.09)	0.11 (0.01)	0.02	7.5
	$J = 7/2$–$5/2$, $F = 4$–3	0.17	0.54 (0.07)	0.10 (0.01)	0.02	7.5
NGC 1333-13	$J = 5/2$–$3/2$, $F = 2$–1	0.14	0.53 (0.10)	0.08 (0.01)	0.02	7.5
	$J = 5/2$–$3/2$, $F = 3$–2	0.24	0.48 (0.06)	0.12 (0.01)	0.02	7.5
	$J = 7/2$–$5/2$, $F = 3$–2	0.29	0.48 (0.05)	0.15 (0.01)	0.02	7.5
	$J = 7/2$–$5/2$, $F = 4$–3	0.35	0.60 (0.05)	0.22 (0.01)	0.02	7.5
NGC 1333-14	$J = 5/2$–$3/2$, $F = 2$–1	0.13	1.15 (0.16)	0.16 (0.02)	0.02	7.9
	$J = 5/2$–$3/2$, $F = 3$–2	0.29	0.70 (0.05)	0.21 (0.01)	0.02	7.9
	$J = 7/2$–$5/2$, $F = 3$–2	0.26	0.76 (0.06)	0.21 (0.01)	0.02	7.8
	$J = 7/2$–$5/2$, $F = 4$–3	0.35	0.68 (0.04)	0.25 (0.01)	0.02	7.8
NGC 1333-15	$J = 5/2$–$3/2$, $F = 3$–2	0.10	0.87 (0.17)	0.09 (0.02)	0.02	8.3
	$J = 7/2$–$5/2$, $F = 3$–2	0.10	0.96 (0.14)	0.10 (0.01)	0.02	8.2
	$J = 7/2$–$5/2$, $F = 4$–3	0.12	0.61 (0.10)	0.08 (0.01)	0.02	8.2
NGC 1333-16	$J = 5/2$–$3/2$, $F = 2$–1	0.10	1.36 (0.78)	0.14 (0.03)	0.02	6.6
	$J = 5/2$–$3/2$, $F = 3$–2	0.14	2.34 (0.78)	0.35 (0.03)	0.02	6.2

Table 6
(Continued)

IDs	Transition J, F	T_{MB}[a] (K)	dv (km s^{-1})	$\int T_{MB} dv$ (K km s^{-1})	rms[b] (K)	V_{LSR} (km s^{-1})
	$J = 7/2–5/2$, $F = 3–2$	0.14	1.85 (0.78)	0.28 (0.03)	0.02	6.5
	$J = 7/2–5/2$, $F = 4–3$	0.20	2.41 (0.78)	0.51 (0.03)	0.02	6.3
NGC 1333-17	$J = 5/2–3/2$, $F = 2–1$	0.86	1.01 (0.20)	0.97 (0.05)	0.04	8.7
	$J = 5/2–3/2$, $F = 3–2$	1.15	1.13 (0.20)	1.38 (0.05)	0.04	8.7
	$J = 7/2–5/2$, $F = 3–2$	1.24	1.07 (0.20)	1.40 (0.05)	0.04	8.7
	$J = 7/2–5/2$, $F = 4–3$	1.54	1.12 (0.20)	1.84 (0.05)	0.04	8.7
L1448-1	$J = 5/2–3/2$, $F = 2–1$	0.44	1.44 (0.06)	0.68 (0.02)	0.03	4.0
	$J = 5/2–3/2$, $F = 3–2$	0.66	1.48 (0.05)	1.05 (0.03)	0.03	4.0
	$J = 7/2–5/2$, $F = 3–2$	0.74	1.38 (0.04)	1.09 (0.03)	0.03	4.0
	$J = 7/2–5/2$, $F = 4–3$	0.86	1.56 (0.04)	1.42 (0.03)	0.03	3.9
L1448-2	$J = 5/2–3/2$, $F = 2–1$	1.01	1.70 (0.22)	1.83 (0.07)	0.03	4.8
	$J = 5/2–3/2$, $F = 3–2$	1.33	1.72 (0.22)	2.44 (0.07)	0.03	4.8
	$J = 7/2–5/2$, $F = 3–2$	1.36	1.80 (0.22)	2.61 (0.07)	0.03	4.8
	$J = 7/2–5/2$, $F = 4–3$	1.59	1.85 (0.22)	3.12 (0.07)	0.03	4.7
L1448-3	$J = 5/2–3/2$, $F = 2–1$	0.45	1.03 (0.06)	0.50 (0.02)	0.03	5.1
	$J = 5/2–3/2$, $F = 3–2$	0.71	0.96 (0.04)	0.73 (0.02)	0.03	5.2
	$J = 7/2–5/2$, $F = 3–2$	0.77	0.98 (0.03)	0.81 (0.02)	0.03	5.2
	$J = 7/2–5/2$, $F = 4–3$	0.93	1.09 (0.03)	1.08 (0.02)	0.03	5.1
L1448-4	$J = 5/2–3/2$, $F = 2–1$	1.05	0.89 (0.02)	0.99 (0.02)	0.03	4.0
	$J = 5/2–3/2$, $F = 3–2$	1.36	0.91 (0.02)	1.33 (0.02)	0.03	4.1
	$J = 7/2–5/2$, $F = 3–2$	1.45	0.96 (0.02)	1.47 (0.02)	0.03	4.0
	$J = 7/2–5/2$, $F = 4–3$	1.58	0.98 (0.01)	1.65 (0.01)	0.03	4.0
L1448-5	$J = 5/2–3/2$, $F = 2–1$	0.22	0.57 (0.12)	0.13 (0.03)	0.05	4.1
	$J = 5/2–3/2$, $F = 3–2$	0.35	0.61 (0.08)	0.23 (0.03)	0.05	4.1
	$J = 7/2–5/2$, $F = 3–2$	0.38	0.50 (0.08)	0.20 (0.03)	0.05	4.2
	$J = 7/2–5/2$, $F = 4–3$	0.40	0.87 (0.08)	0.37 (0.03)	0.05	4.2
IC 348-1	$J = 5/2–3/2$, $F = 2–1$	0.60	0.78 (0.04)	0.49 (0.02)	0.03	9.1
	$J = 5/2–3/2$, $F = 3–2$	0.75	0.82 (0.03)	0.65 (0.02)	0.03	9.1
	$J = 7/2–5/2$, $F = 3–2$	0.81	0.80 (0.03)	0.69 (0.02)	0.03	9.1
	$J = 7/2–5/2$, $F = 4–3$	1.03	0.83 (0.02)	0.91 (0.02)	0.03	9.0
IC 348-2	$J = 5/2–3/2$, $F = 2–1$	0.61	1.00 (0.03)	0.66 (0.02)	0.02	8.6
	$J = 5/2–3/2$, $F = 3–2$	0.85	1.03 (0.02)	0.93 (0.02)	0.02	8.7
	$J = 7/2–5/2$, $F = 3–2$	0.89	1.03 (0.02)	0.97 (0.02)	0.02	8.6
	$J = 7/2–5/2$, $F = 4–3$	1.08	1.03 (0.02)	1.19 (0.02)	0.02	8.6
IC 348-3	$J = 5/2–3/2$, $F = 2–1$	0.16	0.97 (0.11)	0.16 (0.02)	0.02	10
	$J = 5/2–3/2$, $F = 3–2$	0.23	1.45 (0.12)	0.24 (0.02)	0.02	10
	$J = 7/2–5/2$, $F = 3–2$	0.26	1.01 (0.06)	0.28 (0.02)	0.02	10
	$J = 7/2–5/2$, $F = 4–3$	0.32	1.19 (0.07)	0.41 (0.02)	0.02	10
IC 348-4	$J = 5/2–3/2$, $F = 2–1$	0.45	0.82 (0.04)	0.39 (0.02)	0.02	8.5
	$J = 5/2–3/2$, $F = 3–2$	0.70	0.82 (0.02)	0.61 (0.02)	0.02	8.5
	$J = 7/2–5/2$, $F = 3–2$	0.70	0.83 (0.03)	0.60 (0.02)	0.02	8.5
	$J = 7/2–5/2$, $F = 4–3$	0.95	0.84 (0.02)	0.85 (0.02)	0.02	8.5
Barnard 5	$J = 5/2–3/2$, $F = 2–1$	0.81	0.77 (0.02)	0.66 (0.02)	0.03	10
	$J = 5/2–3/2$, $F = 3–2$	1.13	0.77 (0.02)	0.93 (0.02)	0.03	10
	$J = 7/2–5/2$, $F = 3–2$	1.12	0.82 (0.02)	0.98 (0.02)	0.03	10
	$J = 7/2–5/2$, $F = 4–3$	1.38	0.85 (0.02)	1.24 (0.02)	0.03	10
B1-1	$J = 5/2–3/2$, $F = 2–1$	0.27	1.06 (0.09)	0.30 (0.02)	0.03	6.4
	$J = 5/2–3/2$, $F = 3–2$	0.41	0.92 (0.07)	0.40 (0.02)	0.03	6.3
	$J = 7/2–5/2$, $F = 3–2$	0.43	1.01 (0.07)	0.46 (0.02)	0.03	6.4
	$J = 7/2–5/2$, $F = 4–3$	0.54	1.04 (0.06)	0.60 (0.02)	0.03	6.3
B1-2	$J = 5/2–3/2$, $F = 2–1$	0.74	0.62 (0.02)	0.49 (0.01)	0.03	6.6
	$J = 5/2–3/2$, $F = 3–2$	0.92	0.67 (0.02)	0.65 (0.02)	0.03	6.6
	$J = 7/2–5/2$, $F = 3–2$	0.97	0.61 (0.02)	0.63 (0.01)	0.03	6.6
	$J = 7/2–5/2$, $F = 4–3$	1.07	0.66 (0.02)	0.76 (0.02)	0.03	6.6
B1-3	$J = 5/2–3/2$, $F = 2–1$	0.27	1.20 (0.10)	0.34 (0.02)	0.03	6.4
	$J = 5/2–3/2$, $F = 3–2$	0.39	1.08 (0.06)	0.45 (0.02)	0.03	6.3
	$J = 7/2–5/2$, $F = 3–2$	0.39	1.59 (0.11)	0.65 (0.03)	0.03	6.4
	$J = 7/2–5/2$, $F = 4–3$	0.57	0.93 (0.04)	0.57 (0.02)	0.03	6.3
B1-4	$J = 5/2–3/2$, $F = 2–1$	0.50	0.98 (0.22)	0.52 (0.03)	0.03	6.9
	$J = 5/2–3/2$, $F = 3–2$	0.71	1.04 (0.22)	0.78 (0.03)	0.03	6.9

Table 6
(Continued)

IDs	Transition J, F	T_{MB}[a] (K)	dv (km s^{-1})	$\int T_{MB} dv$ (K km s^{-1})	rms[b] (K)	V_{LSR} (km s^{-1})
	$J = 7/2–5/2$, $F = 3–2$	0.77	1.03 (0.22)	0.85 (0.03)	0.03	6.9
	$J = 7/2–5/2$, $F = 4–3$	0.92	1.05 (0.22)	1.02 (0.03)	0.03	6.8
B1-5	$J = 5/2–3/2$, $F = 2–1$	0.29	0.82 (0.07)	0.25 (0.02)	0.03	7.0
	$J = 5/2–3/2$, $F = 3–2$	0.40	0.76 (0.04)	0.32 (0.02)	0.03	7.0
	$J = 7/2–5/2$, $F = 3–2$	0.41	0.96 (0.06)	0.41 (0.02)	0.03	7.0
	$J = 7/2–5/2$, $F = 4–3$	0.50	0.90 (0.05)	0.48 (0.02)	0.03	7.0
L1455-1	$J = 5/2–3/2$, $F = 2–1$	0.43	0.72 (0.22)	0.33 (0.02)	0.02	5.2
	$J = 5/2–3/2$, $F = 3–2$	0.59	0.81 (0.22)	0.50 (0.02)	0.02	5.2
	$J = 7/2–5/2$, $F = 3–2$	0.63	0.81 (0.22)	0.54 (0.02)	0.02	5.2
	$J = 7/2–5/2$, $F = 4–3$	0.69	0.87 (0.22)	0.63 (0.02)	0.02	5.2
L1455-2	$J = 5/2–3/2$, $F = 2–1$	0.52	1.09 (0.04)	0.61 (0.02)	0.03	4.9
	$J = 5/2–3/2$, $F = 3–2$	0.69	1.15 (0.03)	0.84 (0.02)	0.03	4.9
	$J = 7/2–5/2$, $F = 3–2$	0.80	1.12 (0.03)	0.96 (0.02)	0.03	4.9
	$J = 7/2–5/2$, $F = 4–3$	0.96	1.20 (0.03)	1.23 (0.02)	0.03	4.9
L1455-3	$J = 5/2–3/2$, $F = 2–1$	0.43	0.79 (0.04)	0.36 (0.02)	0.03	4.8
	$J = 5/2–3/2$, $F = 3–2$	0.66	0.75 (0.03)	0.52 (0.02)	0.03	4.8
	$J = 7/2–5/2$, $F = 3–2$	0.67	0.73 (0.03)	0.52 (0.02)	0.03	4.8
	$J = 7/2–5/2$, $F = 4–3$	0.88	0.75 (0.02)	0.71 (0.02)	0.03	4.7
L1455-4	$J = 5/2–3/2$, $F = 2–1$	0.23	1.01 (0.08)	0.25 (0.02)	0.03	5.3
	$J = 5/2–3/2$, $F = 3–2$	0.32	1.00 (0.06)	0.33 (0.02)	0.03	5.3
	$J = 7/2–5/2$, $F = 3–2$	0.35	1.09 (0.06)	0.40 (0.02)	0.03	5.3
	$J = 7/2–5/2$, $F = 4–3$	0.44	1.08 (0.05)	0.50 (0.02)	0.03	5.2

Notes.
[a] Obtained by the Gaussian fit.
[b] The rms noise averaged over the line width.

component of C_2H in Table 2 in order to avoid the possible saturation effect as much as possible. Since broad wing components of the CH_3OH lines would likely originate from outflow shocks, we need to exclude them to discuss the chemical compositions of protostellar envelopes. For this purpose, the C_2H velocity width (a full width at half maximum, FWHM) is employed as the velocity range for the integrated intensities of the CH_3OH lines. We use this simple procedure because fitting by a double (or multiple) Gaussian function does not always work, due to asymmetric line profiles. The result is shown in Figure 5(a). The intensities vary over one or two orders of magnitude among the sources, and no correlation can be seen between the C_2H and CH_3OH intensities. Indeed, the correlation coefficient is 0.04 for Figure 5(a), where the upper limits are not involved in the calculation of the correlation coefficient. The C_2H/CH_3OH integrated intensity ratio differs at most by a factor of 100. Even if we focus on only the sources in the NGC 1333 cloud, the correlation plot still shows a large scatter (Figure 5(a)).

For reference, we prepare the same plot sing the integrated intensities of CH_3OH including the wing components, as shown in Figure 5(b). The plots with and without the wing component of CH_3OH do not differ from each other as a whole. In general, CH_3OH is not only abundant in hot inner envelopes but also in outflow-shocked regions (Bachiller et al. 1998). CH_3OH is formed through hydrogenation of CO depleted on a grain mantle in a cold starless phase (e.g., Tielens & Hagen 1982; Watanabe & Kouchi 2002; Soma et al. 2015), and is liberated into the gas-phase in hot regions ($T > 100$ K) or in outflow-shocked regions (e.g., Bachiller & Pérez Gutiérrez 1997; Saruwatari et al. 2011). Furthermore, it can also be liberated even in cold regions to some extent, through non-thermal desorption processes (e.g., Bizzocchi et al. 2014; Soma et al. 2015; Spezzano et al. 2016a, 2016b). For this reason, abundant CH_3OH in the gas-phase means abundant CH_3OH in grain a mantle just before the onset of star formation, whatever its liberation mechanism is. Conversely, CH_3OH cannot be abundant in the gas-phase, if it is deficient on a grain mantle. Indeed, the CH_3OH emission is faint in the WCCC source, L1527, even for the outflow components (e.g., Sakai et al. 2014a; Takakuwa et al. 2000). Hence, the inclusion of the wing components originating from the outflow-shocked regions in the integrated intensity of CH_3OH will not seriously affect the trend that CH_3OH is abundant in the source. However, we use the integrated intensity without the wing components in the following discussion for fair comparison, as stated above.

In addition, the correlation plot of integrated intensities of the CH_3OH and c-C_3H_2 ($3_{2,1}$–$2_{1,2}$, $E_u = 18$ K) lines is shown (see Figure 5(c)). No correlation can be found in this plot, similar to the correlation plot between the integrated intensities of C_2H and CH_3OH. The correlation coefficient is 0.04.

In contrast, the integrated intensities of the C_2H ($N = 3–2$, $J = 5/2–3/2$, $F = 3–2$, $E_u = 25$ K) and c-C_3H_2 ($3_{2,1}$–$1_{1,2}$, $E_u = 18$ K) lines are correlated with each other (see Figure 5(d)). The correlation coefficient is 0.75, where the upper limit values are not included. Although C_2H is thought to be the photodissociation region (PDR) tracer (e.g., Cuadrado et al. 2015), the clear correlation between C_2H and c-C_3H_2 implies that the C_2H lines trace the dense core rather than the PDRs in this study (See Section 4.1).

The correlation of C_2H and c-C_3H_2 has been reported for diffuse clouds and PDRs (e.g., Gerin et al. 2011; Guzmán et al. 2015). In addition, C_2H and c-C_3H_2 exist in dense clouds,

Table 7
Line Parameters of the c-C_3H_2 ($3_{2,1}$–$2_{1,2}$) Lines Observed with IRAM 30 m

IDs	T_{MB}[a] (K)	dv (km s^{-1})	$\int T_{MB} dv$ (K km s^{-1})	rms[b] (K)	V_{LSR} (km s^{-1})
NGC 1333-1	0.23	0.35 (0.08)	0.08 (0.02)	0.04	6.5
NGC 1333-2	0.25	1.03 (0.10)	0.27 (0.02)	0.03	7.5
NGC 1333-3	0.18	0.64 (0.08)	0.12 (0.02)	0.03	8.1
NGC 1333-4	0.09	0.72 (0.26)	0.07 (0.02)	0.03	8.6
NGC 1333-5	0.17	0.69 (0.12)	0.13 (0.02)	0.03	7.7
NGC 1333-6	0.66	0.67 (0.03)	0.47 (0.02)	0.03	7.3
NGC 1333-7	0.21	0.60 (0.08)	0.14 (0.02)	0.03	8.1
NGC 1333-8	0.11	0.90 (0.21)	0.11 (0.02)	0.03	6.6
NGC 1333-9	⋯	⋯	<0.04	0.03	⋯
NGC 1333-10	⋯	⋯	<0.04	0.02	⋯
NGC 1333-11	0.11	0.41 (0.11)	0.05 (0.01)	0.02	8.4
NGC 1333-12	⋯	⋯	<0.03	0.02	⋯
NGC 1333-13	⋯	⋯	<0.03	0.02	⋯
NGC 1333-14	0.12	0.60 (0.11)	0.07 (0.01)	0.02	7.7
NGC 1333-15	⋯	⋯	<0.03	0.02	⋯
NGC 1333-16	0.12	0.72 (0.08)	0.10 (0.01)	0.08	6.8
NGC 1333-17	0.15	1.12 (0.04)	0.18 (0.01)	0.04	8.4
L1448-1	0.50	1.22 (0.06)	0.66 (0.03)	0.04	4.2
L1448-2	0.39	1.34 (0.07)	0.55 (0.03)	0.03	4.6
L1448-3	0.25	0.97 (0.10)	0.26 (0.02)	0.03	4.8
L1448-4	0.39	0.52 (0.04)	0.22 (0.02)	0.03	4.0
L1448-5	0.33	0.46 (0.05)	0.16 (0.02)	0.03	4.1
IC 348-1	0.37	0.61 (0.05)	0.24 (0.02)	0.03	9.0
IC 348-2	0.47	0.56 (0.03)	0.28 (0.01)	0.02	8.8
IC 348-3	⋯	⋯	<0.04	0.02	⋯
IC 348-4	0.28	0.52 (0.04)	0.15 (0.01)	0.02	8.5
Barnard 5	0.22	0.89 (0.10)	0.21 (0.02)	0.02	10
B1-1	0.31	0.89 (0.05)	0.29 (0.02)	0.02	6.3
B1-2	0.36	0.65 (0.05)	0.25 (0.02)	0.02	6.5
B1-3	0.13	0.99 (0.15)	0.13 (0.02)	0.03	6.3
B1-4	0.36	0.75 (0.06)	0.28 (0.02)	0.03	6.9
B1-5	0.20	0.53 (0.06)	0.11 (0.02)	0.03	6.9
L1455-1	0.28	0.53 (0.04)	0.16 (0.01)	0.02	5.2
L1455-2	0.19	1.01 (0.13)	0.20 (0.02)	0.02	5.0
L1455-3	0.19	0.51 (0.07)	0.10 (0.01)	0.03	4.8
L1455-4	0.10	0.35 (0.17)	0.03 (0.01)	0.02	5.1

Notes. The errors are 1σ. The upper limit to the integrated intensity is calculated as $\int T_{MB} dv < 3\sigma \times \sqrt{(dv/dv_{res})}\, dv_{res}$, where dv is the assumed line width (0.8 km s^{-1}) and dv_{res} is the velocity resolution per channel.
[a] Obtained by the Gaussian fit.
[b] The rms noise averaged over the line width.

including starless cores and protostellar cores (e.g., Sakai et al. 2008, 2014a; Koumpia et al. 2016, 2017). Since we observed the high excitation lines of C_2H and c-C_3H_2 toward the protostellar cores at almost the same distance, our result suggests that the correlation between the two lines holds in protostellar cores, as expected from carbon chemistry in dense clouds (Sakai & Yamamoto 2013; Yamamoto 2017). In contrast, Fontani et al. (2012) presented anti-correlation between the two molecules, C_2H and c-C_3H_2 in a UC H II region, suggesting a complex physical structure for the source.

3.3. Derivation of Rotation Temperatures and Column Densities

To investigate the chemical diversity, we derive the beam-averaged column densities of CH_3OH, C_2H, and c-C_3H_2 under the assumption of local thermodynamic equilibrium (LTE) conditions. The rotation temperature of CH_3OH (E state) was evaluated from the multiple transition lines with different upper state energies, where a rotational diagram method assuming optically thin emission was used (e.g., Watanabe et al. 2015). We used the E state lines, because more lines are available than for the A state. Examples of the rotation diagrams prepared in our analyses are shown in Figure 6 (also see Figure 11).

The derived rotation temperature ranges from 8 to 21 K. The rotation temperatures of CH_3OH, derived for NGC 1333-1 (IRAS 4B), NGC 1333-2 (IRAS 2), L1448-2, and L1448-3 using the K structure lines of the $J = 5$–4 and $J = 7$–6 transition, are lower by 6–82 K than those reported by Maret et al. (2005). Maret et al. (2005) only employed the high excitation lines ($J = 5$–4 and $J = 7$–6) of CH_3OH in their analysis. In contrast, we employ the $J = 2$–1 lines instead of higher excitation lines, which would likely trace CH_3OH not only in a warm and dense part, but also in a colder envelope part. This seems to be a reason for the lower temperature obtained in our study.

It should be noted that we are observing the CH_3OH emission in the protostellar envelope. One may think that the CH_3OH emission mainly comes from the small hot region (∼100 K) near the protostar. However, its contribution may not be dominant in our observations, because the rotation temperature is as low as 8–21 K. Rotation temperatures of 8–21 K are too low to trace hot corinos, even considering that CH_3OH emission is sub-thematically excited (e.g., Bachiller et al. 1998 and references therein). Moreover, we do not find any correlation between the CH_3OH intensity and the protostellar luminosity (Figure 7); higher-luminosity sources do not always give stronger CH_3OH emission in our observation.

The rotation temperature derived by the rotation diagram analysis depends on the assumed source size. If the source size is smaller than the observation beams both for the $J = 2$–1 (97 GHz) and $J = 5$–4 (242 GHz) lines, the rotation temperature derived above would be lower than our estimate, because the beam dilution effect is larger for the 97 GHz observation. If the emitting region is smaller for the 242 GHz line than for the 97 GHz line due to the higher critical density, the beam dilution effect can be larger for the 242 GHz line. In this case, the rotation temperature would be higher than our estimate. Although these two situations may be the case, we do not know the internal structure within the observation beam for individual sources. When the two above limitations are considered, assuming that the beam filling factor is unity provides a moderate estimate of the rotation temperature. Moreover, in the following sections we discuss the results within our sample sources, which are almost equally distant from the Sun. Thus, the systematic errors due to the beam dilution effect would be mitigated to some extent for the column density ratios, which are mainly used in our discussions.

By assuming that the abundance of the A state is the same as that of the E state, the total beam-averaged column density of CH_3OH for each source is determined from the integrated intensities within the velocity range of the C_2H line averaged for the four hyperfine components in order to eliminate the outflow component as much as possible. Since the actual source size is unknown for most of the sources, the beam filling factor of unity is used for simplicity, as discussed above. Thus, the beam-averaged column density is derived in this study. Here, the uncertainties of the derived column densities are evaluated from the rms noise. For C_2H and c-C_3H_2, we used the $N = 3$–2, $J = 5/2$–$3/2$, $F = 3$–2 line and the $3_{2,1}$–$2_{1,2}$ line to derive the beam-averaged column density, respectively, where we assume the rotation

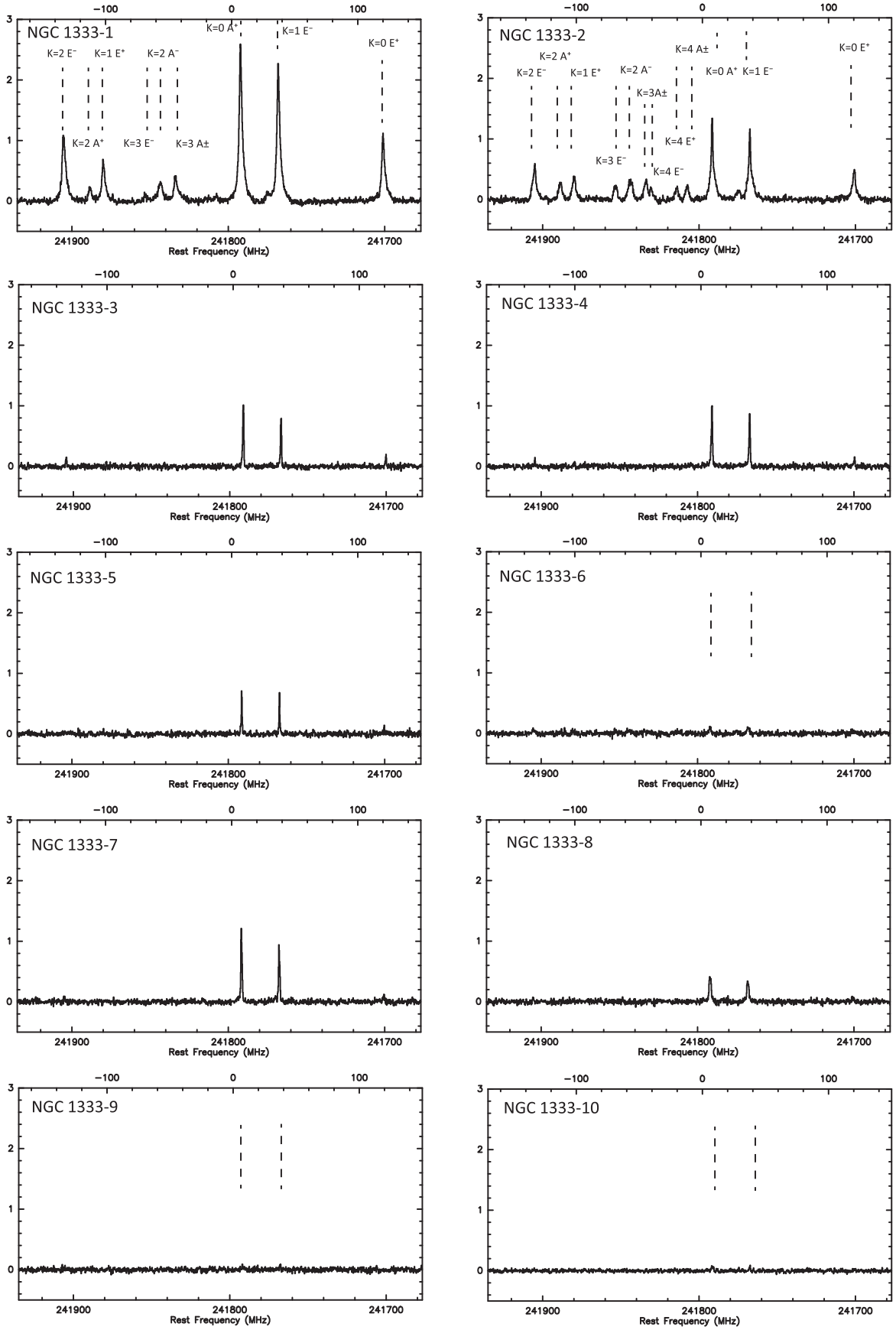

Figure 2. Line profiles of CH_3OH ($J = 5$–4) observed with IRAM 30 m. The spectra taken with the wobbler switching are indicated with an asterisk (ASAI project). (An extended version of this figure is available.)

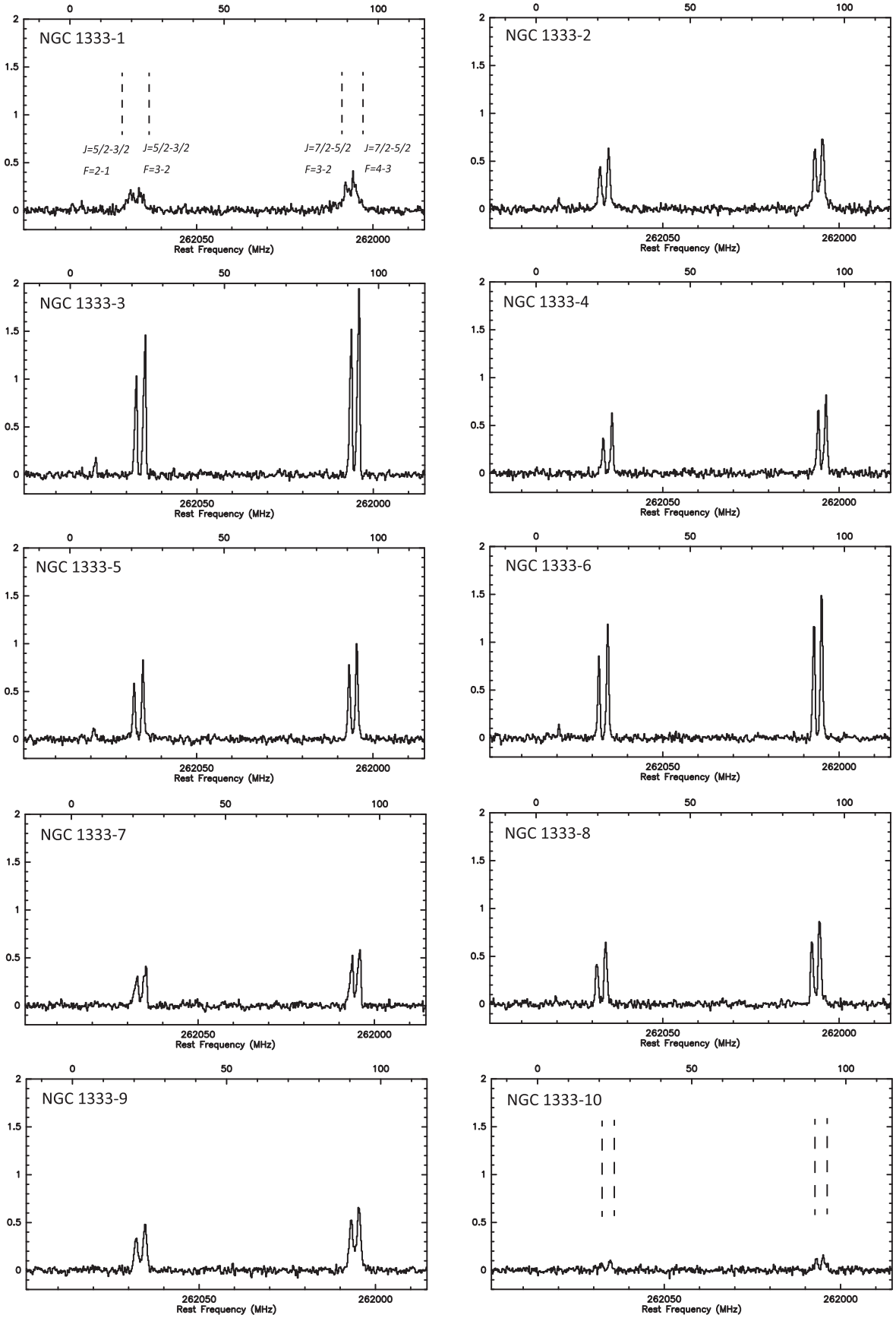

Figure 3. Line profiles of C_2H ($N = 3$–2) observed with IRAM 30 m. The spectra taken with the wobbler switching are indicated with an asterisk (ASAI project). (An extended version of this figure is available.)

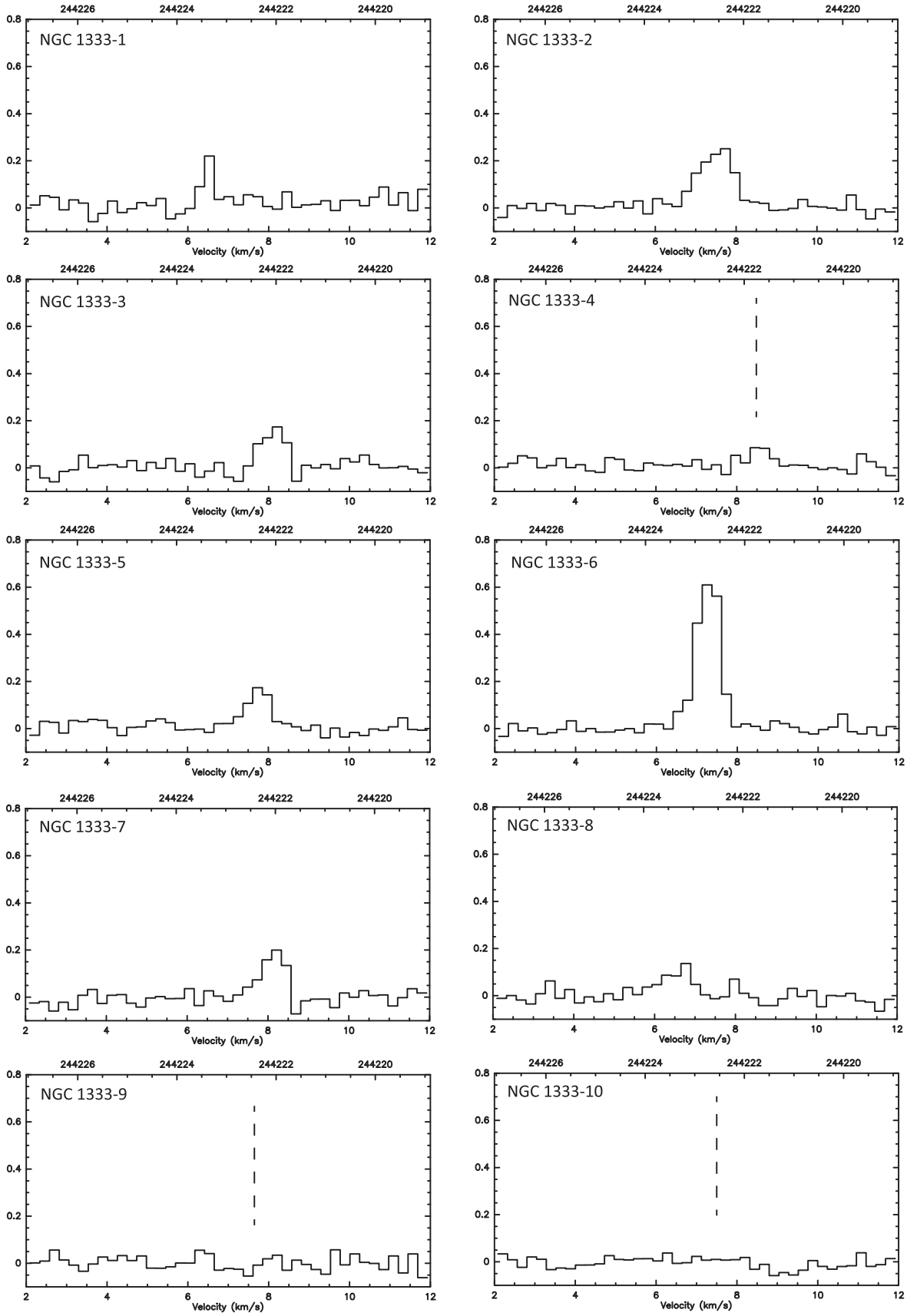

Figure 4. Line profiles of c-C_3H_2 ($3_{2,1}$–$2_{1,2}$) observed with IRAM 30 m. The spectra taken with the wobbler switching are indicated with an asterisk (ASAI project). (An extended version of this figure is available.)

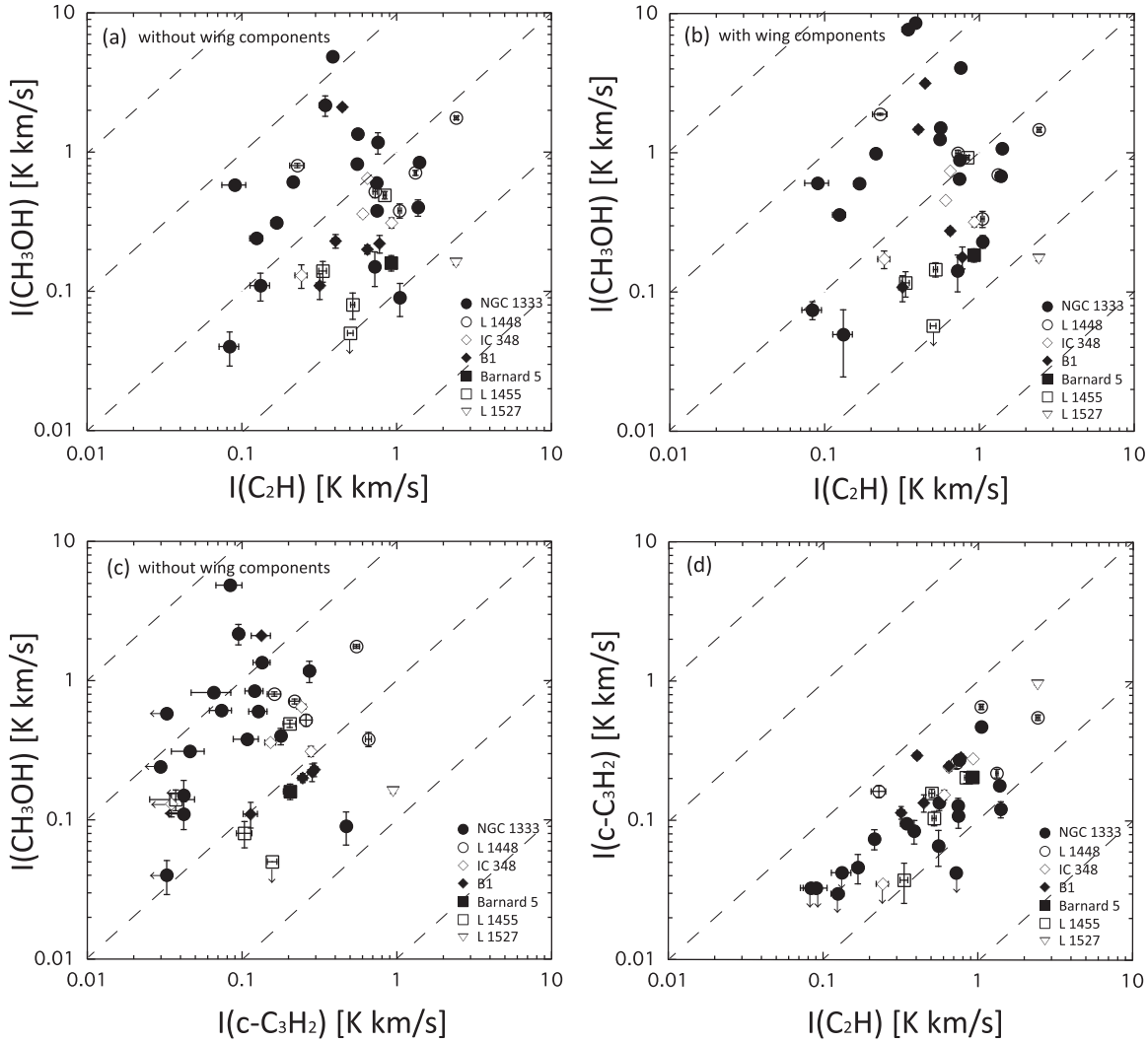

Figure 5. (a) Correlation plot between the integrated intensities of the C_2H ($N = 3$–2, $J = 5/2$–$3/2$, $F = 3$–2) and CH_3OH ($J = 5$–4, $K = 1$, E^-) lines, excluding wing components for the latter (correlation coefficient = 0.04). The dashed lines indicate the intensity ratios of 100, 10, 1, 0.1, and 0.01. (b) Correlation plot between the integrated intensities of the C_2H ($N = 3$–2, $J = 5/2$–$3/2$, $F = 3$–2) and CH_3OH ($J = 5$–4, $K = 1$, E^-) lines, including the wing components for the latter (correlation coefficient = 0.04). The dashed lines indicate the intensity ratios of 100, 10, 1, 0.1, and 0.01. (c) Correlation plot between the integrated intensities of the c-C_3H_2 ($3_{2,1}$–$2_{1,2}$) and CH_3OH ($J = 5$–4, $K = 1$, E^-) lines (correlation coefficient = 0.17). The dashed lines indicate the intensity ratios of 100, 10, 1, 0.1, and 0.01. (d) Correlation plot between the integrated intensities of the C_2H ($N = 3$–2, $J = 5/2$–$3/2$, $F = 3$–2) and c-C_3H_2 ($3_{2,1}$–$2_{1,2}$) lines (correlation coefficient = 0.75). The dashed lines indicate the intensity ratios of 100, 10, 1, 0.1, and 0.01. Data points with an arrow in CH_3OH and c-C_3H_2 intensities show the upper limits. The correlation coefficient is defined as $\Sigma(x_i - \bar{x})(y_i - \bar{y})/\sqrt{\Sigma(x_i - \bar{x})^2\Sigma(y_i - \bar{y})^2}$, where $\bar{x}$ and $\bar{y}$ represent the average values of the data x_i and y_i, respectively.

temperature of CH_3OH derived for each source. Note that for NGC 1333-16 and NGC 1333-17, the rotation temperatures of CH_3OH for the nearby sources, NGC 1333-1 and NGC 1333-2, are employed, respectively, because of the lack of the Nobeyama data. Table 3 summarizes the derived beam-averaged column densities.

NGC 1333-1 (IRAS 4B), NGC 1333-16 (IRAS 4A), NGC 1333-7, and B1-3 show high CH_3OH column densities. On the other hand, L1448-2 shows higher column densities of C_2H and c-C_3H_2, which are about an order of magnitude higher than those in NGC 1333-1, and about a half an order of magnitude higher than those in L1527 (Sakai et al. 2008).

4. Discussion

4.1. Chemical Variation between C_2H and CH_3OH

In this section, we use the beam-averaged column densities summarized in Table 3 to characterize the chemical composition of protostellar sources at a few 1000 au scale. Smaller-scale chemical variation is averaged out, and hence a spatial attention is needed when they are compared with the column densities in other studies at a higher angular resolution or with source-size corrections. Nevertheless, the beam-averaged column densities can be used for mutual comparison among our samples in the Perseus molecular cloud complex, because the sources are at similar distances and the column densities are derived in a uniform way.

Figure 8(a) shows the correlation plot of the beam-averaged column densities between C_2H and CH_3OH, while Figure 8(b) depicts those between C_2H and c-C_3H_2. The column densities of C_2H and c-C_3H_2 correlate with each other, because these two molecules would be produced in related pathways (Sakai & Yamamoto 2013). In contrast, no correlation can be seen between C_2H and CH_3OH in the column densities, similar to the integrated intensities (Figures 5(a) and (b)). Similarly, no correlation is found between c-C_3H_2 and CH_3OH, either, as shown in Figure 5(c).

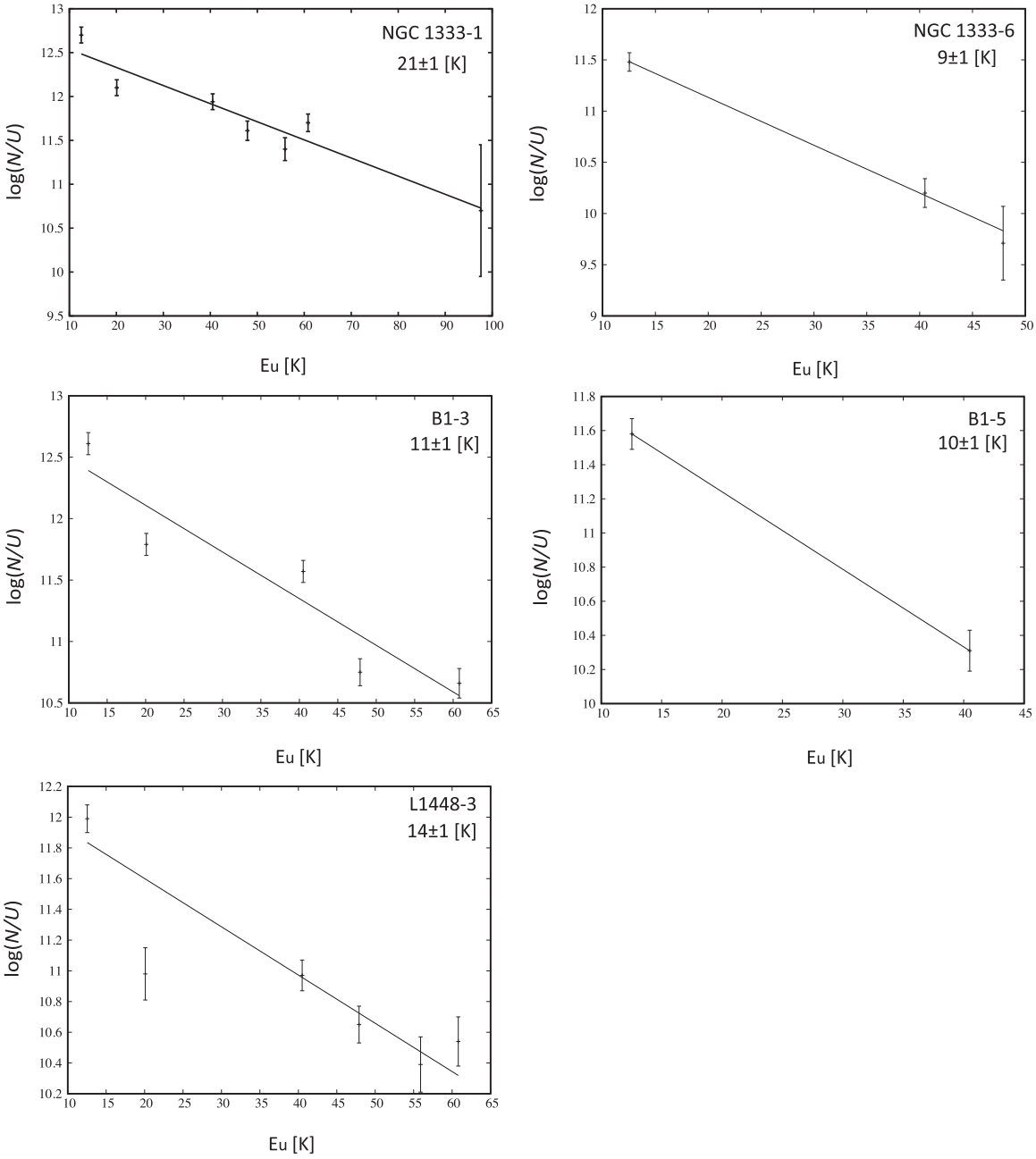

Figure 6. Rotation diagrams of CH_3OH for NGC 1333-1, NGC 1333-6, B1-3, B1-5, and L1448-3.

These results clearly indicate the chemical diversity at a few 1000 au scale around the protostar. The C_2H/CH_3OH ratios range over almost two orders of magnitude even among the Class 0/I sources within the same molecular cloud complex. A similar diversity for the C_4H/CH_3OH ratio among various protostellar sources was also reported by Graninger et al. (2016) and Lindberg et al. (2016). However, our result is the first one based on unbiased samples in the single molecular cloud complex.

It is likely that the above chemical diversity at a few 1000 au scale is related to the chemical diversity identified at a smaller scale; namely, hot corino chemistry and WCCC. As discussed by Sakai et al. (2009) and Sakai & Yamamoto (2013), definitive identification of hot corino chemistry and WCCC requires the confirmation of the central concentration of COMs and carbon-chain molecules, respectively. Such a concentration is not confirmed for C_2H, c-C_3H_2, and CH_3OH in our single-point observations. Nevertheless, it is likely that the beam-averaged chemical composition does reflect the chemical composition of the protostellar core to some extent, because the high excitation lines of CH_3OH, C_2H, and c-C_3H_2 are employed in this study to trace dense regions rather than the component extended over parent molecular clouds.

For NGC 1333-1 (IRAS 4B) and NGC 1333-16 (IRAS 4A), which have previously been identified as hot corino sources, we indeed see abundant CH_3OH but deficient C_2H, their C_2H/CH_3OH column density ratios being almost the lowest among the observed sources (Table 3). On the other hand, the WCCC source L1527 in Taurus, which is employed as a

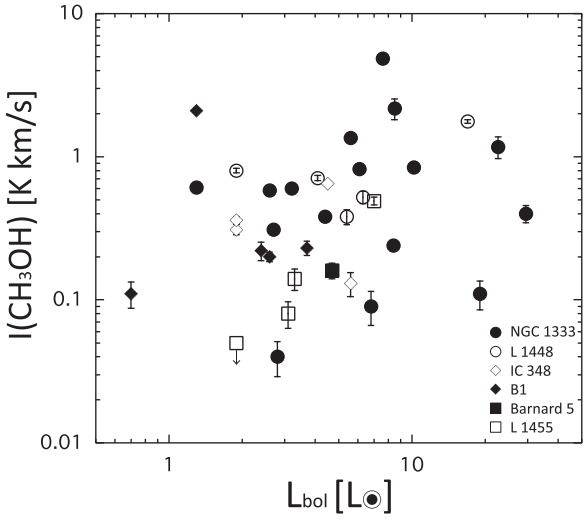

Figure 7. Correlation plot between the integrated intensities of CH_3OH ($J = 5$–4, $K = 1$, E^-) lines, excluding wing components and the protostellar luminosity (correlation coefficient = 0.19). The data point with an arrowed line in the CH_3OH intensity shows the upper limit. The correlation coefficient is defined in the caption in Figure 5.

reference, shows abundant C_2H and deficient CH_3OH with the single-dish observation in the ASAI project (Lefloch et al. 2018), as shown in Figure 9(a). Importantly, most of the sources show the ratios between those of the hot corino sources and the WCCC source. Thus, the hot corino sources and the WCCC source are certainly two extreme cases of chemical variation.

Sakai et al. (2009) and Sakai & Yamamoto (2013) suggested that the difference in the chemical compositions found between WCCC sources and hot corino sources could originate from the different duration times of the starless phase after shielding the interstellar UV radiation in the parent molecular cloud. For efficient formation of various COMs, a significant amount of CH_3OH is necessary as a parent molecule (e.g., Garrod & Herbst 2006). CH_3OH is mainly formed by hydrogenation of CO on a grain mantle (e.g., Tielens & Hagen 1982; Watanabe & Kouchi 2002; Soma et al. 2015). On the other hand, it takes about 10^{5-6} years for the formation of CH_3OH from CO, if the H_2 density of the parent cloud is as high as 10^5 cm^{-3} (Taquet et al. 2012). When the core-collapse starts well after the shielding of the interstellar UV radiation in the parent cloud, most of the carbon atoms are fixed into CO by gas-phase reactions, and CO is depleted onto dust grains in dense and cold regions to form CH_3OH.

On the other hand, there is not enough time for the C to CO conversion in the gas-phase, if the core-collapse starts just after the UV-shielding. Carbon atoms can still be abundant in such cores. The timescale for the depletion of atoms and molecules onto dust grains is roughly $10^5/(n/10^4\,\mathrm{cm}^{-3})$ yr (e.g., Burke & Hollenbach 1983), which is comparable to the dynamical timescale. Hence, carbon atom is depleted onto dust grains before it is converted to CO by gas-phase reactions. Hydrogenation of C on grain surfaces forms CH_4 efficiently. After the onset of star formation, CH_4 is evaporated into the gas-phase in a warm region ($T > 25$ K) to form various carbon-chain molecules through gas-phase reactions (i.e., the WCCC mechanism). In this case, the core-collapse occurs in chemically young clouds, hence carbon-chain molecules produced in the early evolutionary stage of cold starless cores could also survive in the gas-phase to some extent.

In L1527, a cold envelope with abundant carbon-chain molecules surrounds the dense ($n \sim 10^6\,\mathrm{cm}^{-3}$) and warm ($T > 25$ K) core where the enhancement of carbon-chain molecules due to WCCC is occurring (Sakai et al. 2010). In contrast, carbon-chain molecules are relatively deficient in hot corino sources even in the surrounding component (e.g., Sakai & Yamamoto 2013). Therefore, the ratios between carbon-chain molecules, especially C_nH and C_nH_2, and CH_3OH, are expected to represent the chemical characteristics of protostellar cores, even if a part of the observed emission comes from outflows or cold dense envelopes in addition to that from the inner part of protostellar cores.

It should be noted that C_2H is known to be abundant in PDRs (e.g., Pety et al. 2007; Cuadrado et al. 2015). In such regions, C_2H is efficiently produced from C^+ in the gas-phase reaction and/or is formed by destruction of very small grains and polycyclic aromatic hydrocarbons (e.g., Cuadrado et al. 2015). However, we observed the regions with high extinction ($A_v > 5$–7 mag; Kirk et al. 2006) in relatively high critical density lines. Hence, the detected C_2H emissions would mainly originate from protostellar cores rather than to the surrounding diffuse parts to which the UV radiation can penetrate. Nevertheless, C_2H would also exist in the cavity walls of low-velocity outflows, where C_2H could be formed by the UV radiation from the central protostar (e.g., Oya et al. 2014). To assess this effect, we also observed the c-C_3H_2 lines. As demonstrated in Figure 8(b), the column densities of C_2H and c-C_3H_2 show a good correlation. The C_2H/c-C_3H_2 ratio is about 10, which is lower than those found in PDRs and diffuse clouds and is rather close to those of dense cores (Gerin et al. 2011; Cuadrado et al. 2015). In fact, Lindberg et al. (2015) also reported that c-C_3H_2 is not affected by the UV radiation in the R CrA region. Although c-C_3H_2 is detected in the outflow-shocked region L1157 B1 (Yamaguchi et al. 2012), its abundance is not as high as that in the protostellar core of L1157 mm (Bachiller & Pérez Gutiérrez 1997). Above all, the diversity seen in the C_2H/CH_3OH column density ratio most likely reflects the chemical diversity of protostellar cores.

4.2. Effects from the Evolutionary Stage of the Source

Figures 9(a)–(c) show the correlation plots of the C_2H/CH_3OH ratio against the envelope mass M_{env}, the ratio of the bolometric luminosity to the submillimeter wavelength luminosity L_{bol}/L_{smm}, and the bolometric temperature T_{bol}, respectively. The envelope mass (M_{env}) represents the amount of the gas associated with the protostar, whereas L_{bol}/L_{smm} and T_{bol} are known as evolutionary indicators of the protostellar source (Hatchell et al. 2005, 2007).

In Figure 9(a), the M_{env} values are taken from Hatchell et al. (2007). These values are derived from the 850 μm dust continuum flux observed with JCMT, which has a beam size similar to that of our IRAM 30 m observations in the 1.3 mm band ($\sim$15″). The correlation coefficient is 0.02, indicating no correlation. Hence, the result indicates that there is no clear relationship between the chemical composition and the mass to be accreted.

Likewise, L_{bol}/L_{smm} and T_{bol} also do not show a correlation with the C_2H/CH_3OH ratio (Figures 9(b) and (c)), where L_{bol}/L_{smm} and T_{bol} are also taken from Hatchell et al. (2007).

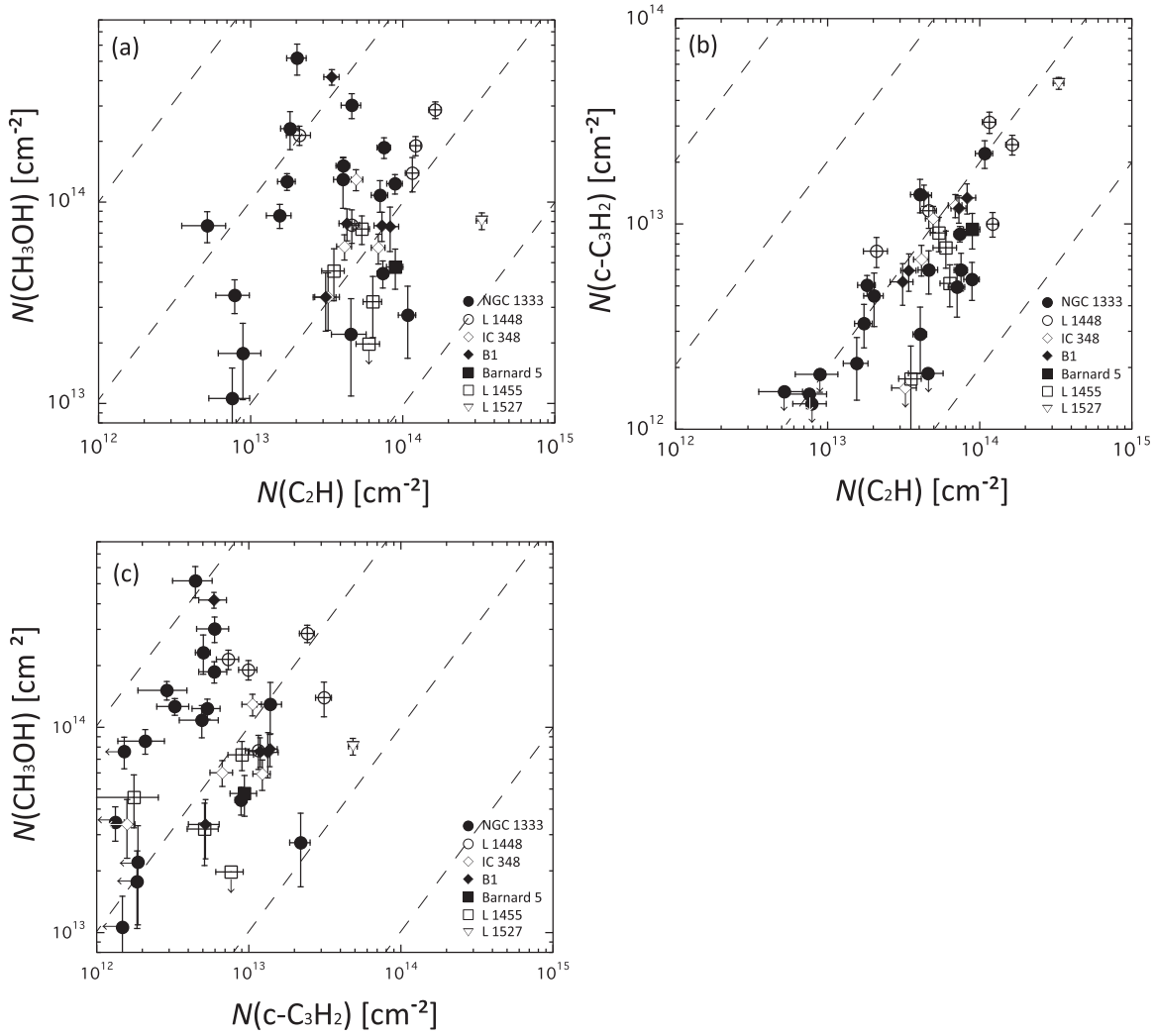

Figure 8. (a) Correlation plot between the column densities of C_2H and CH_3OH (correlation coefficient = 0.01). The dashed lines indicate intensity ratios of 100, 10, 1, and 0.1. (b) Correlation plot between the column densities of C_2H and c-C_3H_2 (correlation coefficient = 0.88). The dashed lines indicate intensity ratios of 100, 10, 1, and 0.1. (c) Correlation plot between the column densities of c-C_3H_2 and CH_3OH (correlation coefficient = 0.1). The dashed lines indicate intensity ratios of 100, 10, 1, and 0.1. Data points with an arrow in CH_3OH and c-C_3H_2 column densities show the upper limits. The correlation coefficient is defined in the caption in Figure 5.

The correlation coefficients for the L_{bol}/L_{smm} and T_{bol} plots are as small as 0.26 and 0.31, respectively. Thus, the evolutionary stage does not show correlation with the C_2H/CH_3OH ratio. This is because the chemical composition of the grain mantles, which characterizes the gas-phase chemical composition after the onset of star formation, has already been determined by the processes during the starless core phase.

4.3. Positional Effects in the Parent Cloud

To test the relation between the positions of protostars and the C_2H/CH_3OH ratios, we introduce the minimum projected distance from the molecular cloud edge, D_{min}, i.e., small D_{min} indicates a source closer to the edge of the cloud. D_{min} is calculated using the Planck 217 GHz continuum map (see Figure 10), where the cloud edge is arbitrarily defined as the 10σ contour. Note that the 10σ contour of the Planck continuum map, which we employ as the edge of the cloud, corresponds to an A_v of 1 mag (Kirk et al. 2006). Figure 9(d) shows the correlation plot of the C_2H/CH_3OH ratio against D_{min}. Note that a typical size of the cloud is 1 pc (e.g., Hacar et al. 2017), hence there is a sharp limit of D_{min} around 0.6–0.7 pc.

D_{min} is a projected distance, and the line-of-sight depth from the cloud surface is unknown. Hence, sources that appear near the center of the cloud are not always embedded deeply in the clouds, but some of them may be close to the cloud periphery along the line of sight. Although D_{min} is affected by this projection effect, we can obtain clues regarding the origin of the chemical diversity from Figure 9(d). These results suggest that the sources with lower ratios tend to appear only at larger D_{min}. Namely, they are likely more embedded in the central part of the large molecular clouds.

Figure 9(d) shows a kind of "right angle" distribution of the points: sources with small D_{min} have only high C_2H/CH_3OH ratios. On the other hand, sources with large D_{min} have both high and low C_2H/CH_3OH ratios, indicating a large scatter of the ratios. Although this scatter mainly comes from the NGC 1333 region, a similar trend can be seen in the plots without the NGC 1333 sources. It should be stressed that there is a blank area in the bottom left corner, where D_{min} is small and the ratio is low.

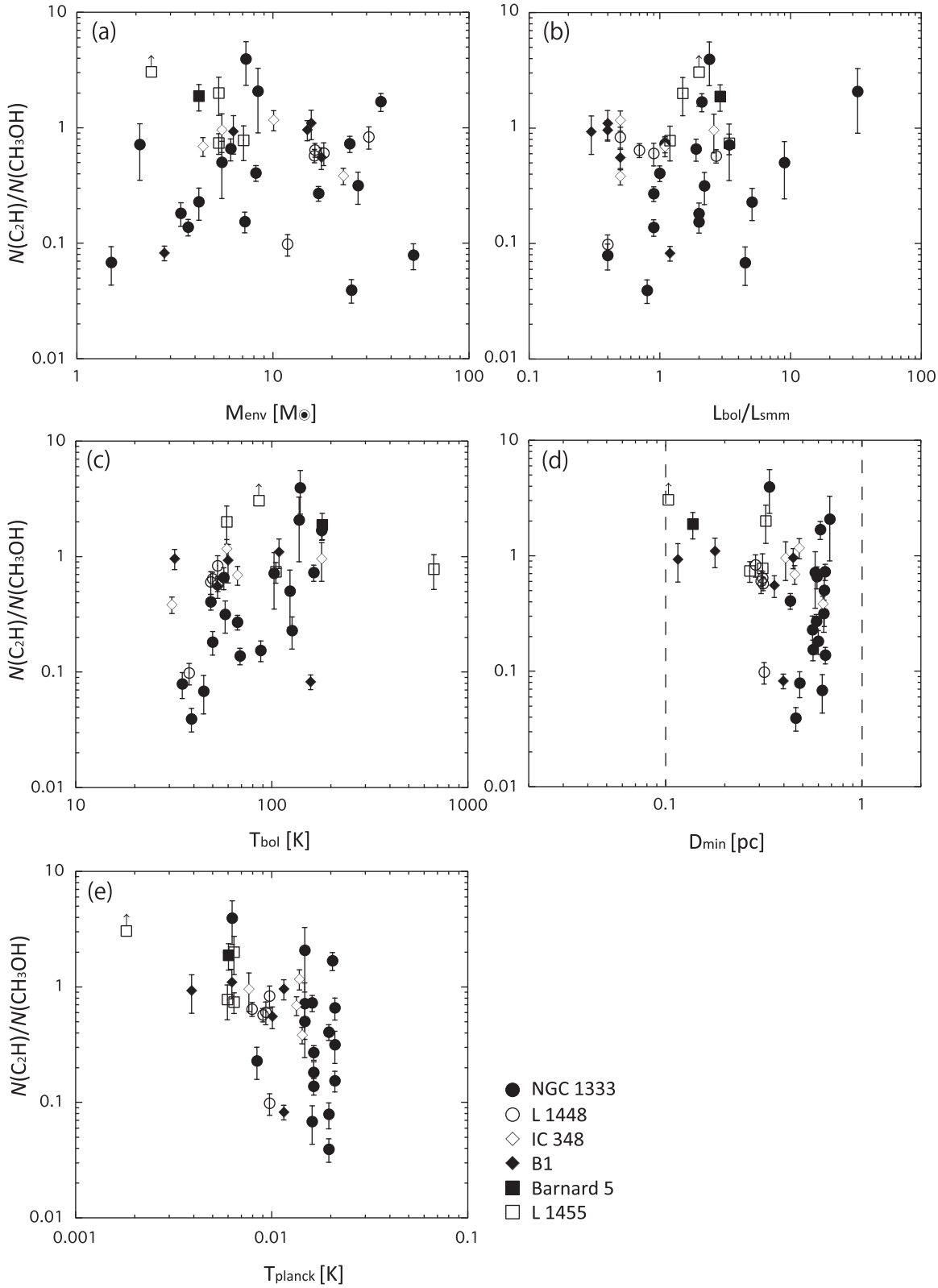

Figure 9. Correlation plot between the C_2H/CH_3OH ratio vs. (a) envelope mass M_{env}(correlation coefficient = 0.02), (b) L_{bol}/L_{smm} (correlation coefficient = 0.26), (c) T_{bol} (correlation coefficient = 0.31), (d) D_{min}, the minimum distance from the source position and cloud edge (correlation coefficient = 0.27), and (e) the peak intensity of the source position from the Planck map (correlation coefficient = 0.42). A dashed line of 0.1 pc shows the spatial resolution of the observations, and the line of 1 pc shows the largest cloud size for (d). Data points with an arrow show the lower limits. The correlation coefficient is defined in the caption in Figure 5. The correlation coefficient is derived excluding the lower limit data. If we include the data point, the correlation coefficient changes to 0.12 for (a), 0.13 for (b), 0.28 for (c), 0.45 for (d), and 0.58 for (e), respectively.

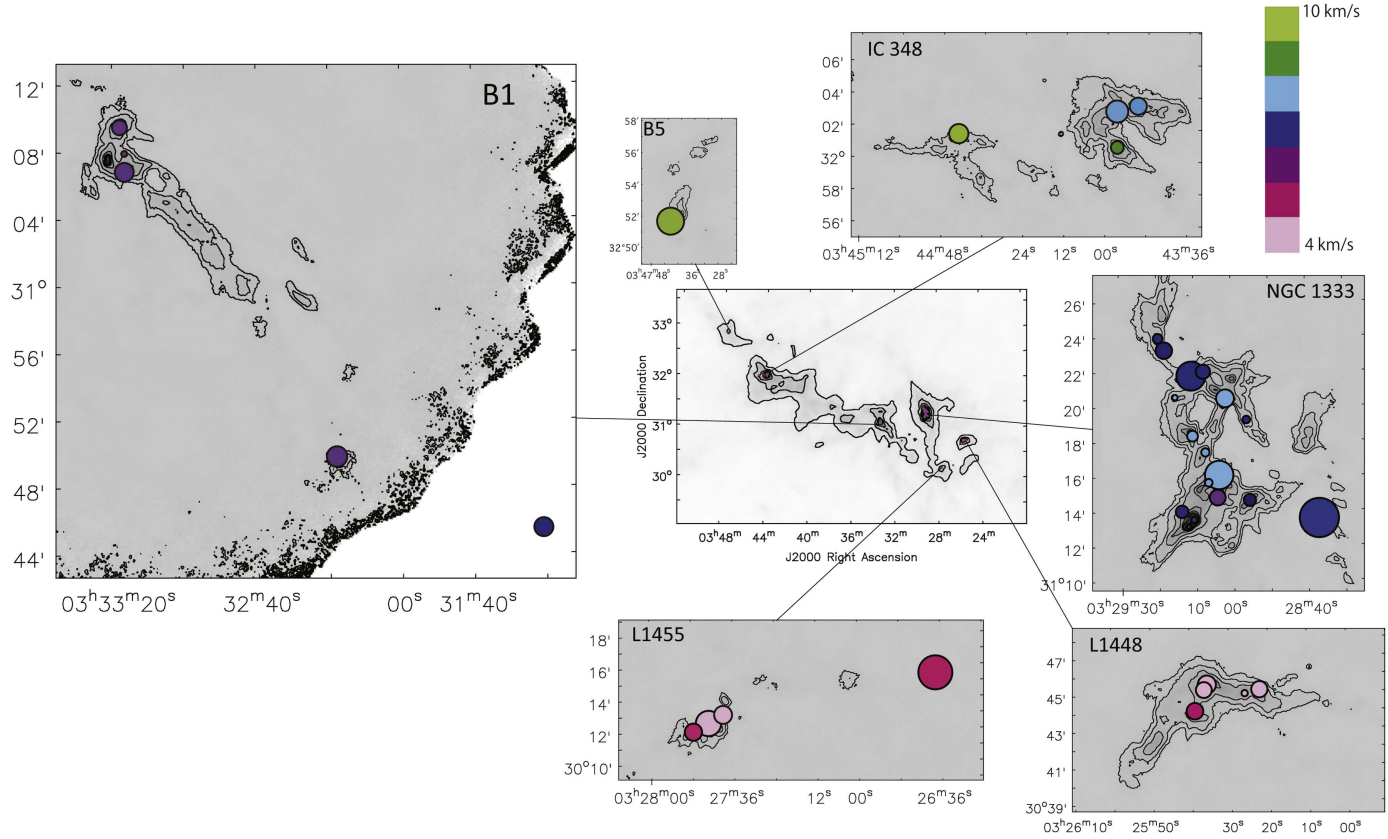

Figure 10. Planck 217 GHz map (central part; contours are 5σ, 10σ, 15σ, 20σ, 25σ, 30σ, 35σ, and 40σ levels, $1\sigma = 0.5$ mK) and SCUBA 850 μm maps of the NGC 1333, L1448, IC 348, B5, B1, and L1455 regions. The grayscale is a 850 μm continuum. The flux is shown on a log scale from 0.5 Jy beam^{-1} to 1.5 Jy beam^{-1}. Contours are 5σ, 10σ, 20σ, 40σ, 60σ, 80σ, 100σ, 200σ, and 400σ levels ($1\sigma = 0.01$ Jy beam^{-1}). The radius of each circle overlaid on the JCMT 850 μm images of the Perseus clouds (Chen et al. 2016) is proportional to the C_2H/CH_3OH ratio. The colors show the systemic velocity of the individual position.

One may think that this is caused by the source selection effect. In our source sample, the very-low-luminosity ($L_{bol} < 1\,L_\odot$) sources are missing. If these sources had a low C_2H/CH_3OH ratio, the blank area might be filled up. However, this would not be the case, because there is no correlation between the luminosity and the C_2H/CH_3OH ratio.

Most of the chemical diversity in our sample is thus concentrated in the large D_{min} region. Since all the sources near the cloud edge (small D_{min} sources) have high ratios, the sources with high ratios at large D_{min} may have a small line-of-sight depth from the cloud surface. Alternatively, substructure (clumpy and/or filamentary structure) in the molecular clouds (e.g., velocity-coherent structures found in NGC 1333 by Hacar et al. 2017) might also contribute to the high ratios because such substructures allow the interstellar UV radiation to penetrate into the cloud (e.g., Stutzki et al. 1988; Meixner & Tielens 1993).

In order to investigate the relation between the C_2H/CH_3OH ratio and the line-of sight depth of the cloud, we prepare the correlation of the ratio against the peak intensity of the Planck continuum map at the source positions, as shown in Figure 9(e). The distribution of the points reveals a trend similar to that found in Figure 9(d). Again, there is a blank area in the bottom left corner, where the peak intensity is low and the ratio is low. The scatter in the high peak intensity region can be interpreted in the same way as that in the large D_{min} case.

In Figure 10, the C_2H/CH_3OH ratio is represented by a radius of the circle, which is overlaid on the JCMT 850 μm images of the Perseus clouds (Chen et al. 2016). Indeed, the high C_2H/CH_3OH ratio sources, i.e., the WCCC-type sources (larger circles), seem to be isolated or located at the edge of the cloud, although NGC 1333-17 (SVS 13A) is an exception. In contrast, the low C_2H/CH_3OH ratio sources, i.e., sources whose chemical character is close to the hot corino sources, tend to be concentrated in the inner regions of the cluster-forming clouds (NGC 1333 and IC 348). This result implies that the isolated sources and the sources in cloud peripheries tend to have the WCCC character in the Perseus molecular cloud complex.

In the central part of the cloud, the time after the UV-shielding would be longer than that in the cloud peripheries, because the surrounding gas gradually contracting to the main body of the cloud can shield the UV radiation. In the cloud center, the carbon atoms have been converted to CO, and CO depletion has already occurred in dense cores. In this case, CH_3OH can be abundant on dust grains, which is reflected in the gas-phase abundance through the thermal and/or non-thermal desorption processes. On the other hand, carbon atoms can be abundant in the cloud peripheries. They can be depleted directly onto dust grains to form CH_4, which leads to WCCC. This picture is consistent with the result in which higher C_2H/CH_3OH and c-C_3H_2/CH_3OH ratios are seen in protostellar cores at the cloud peripheries,

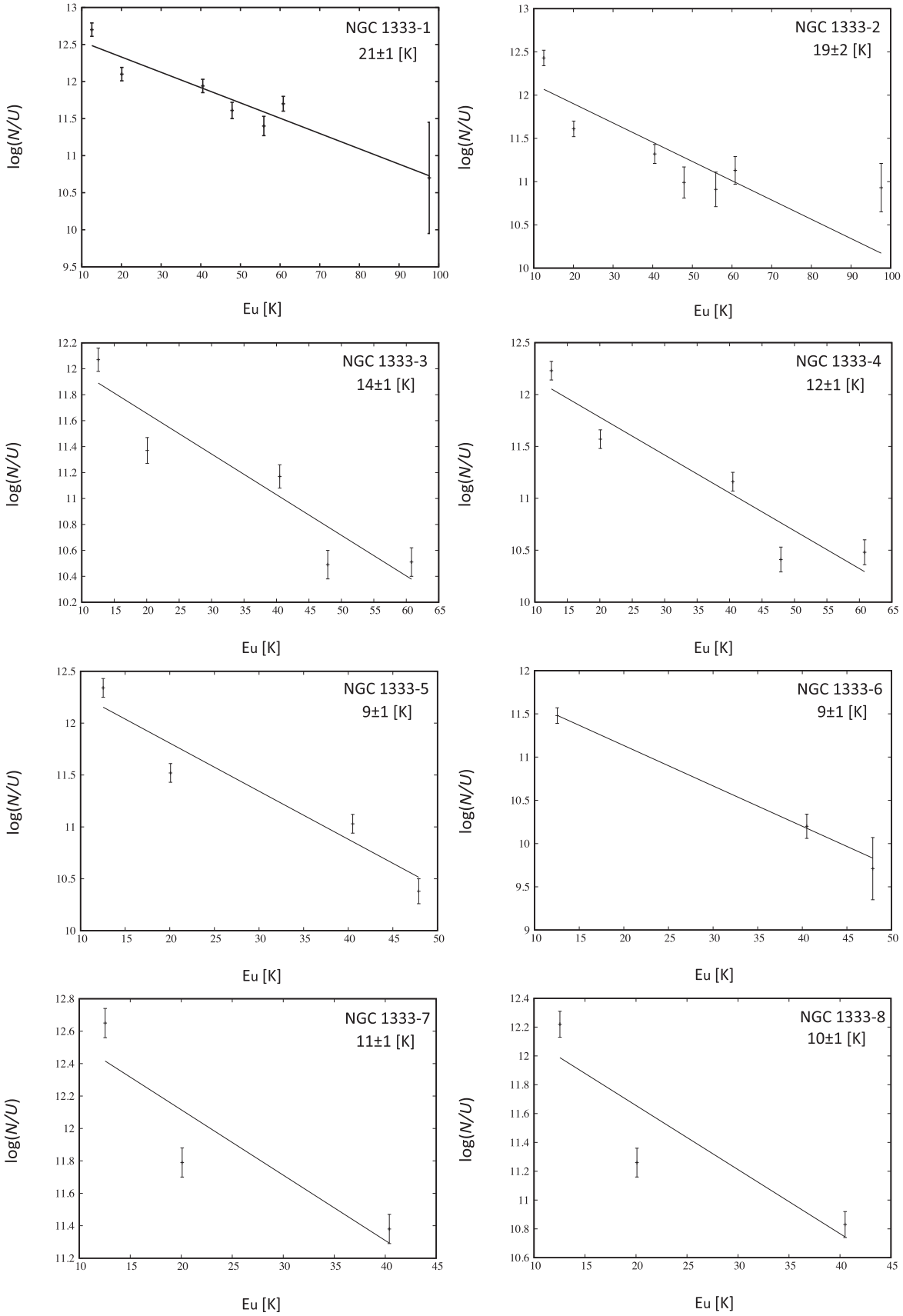

Figure 11. Rotation diagrams of CH_3OH (*E* state). Detected lines are marked by points with error bars. A solid line indicates a single temperature fit. (An extended version of this figure is available.)

whereas low values only appear in the cores at the cloud center.

However, it is not clear at present whether the regeneration mechanism of carbon-chain molecules expected for WCCC is actually occurring in the sources with the high C_2H/CH_3OH and c-C_3H_2/CH_3OH ratios. To assess this point, the central concentration of carbon-chain molecules should be confirmed for each source by high-resolution observations. Moreover, it has recently been revealed that the situation may be more complicated at a smaller scale (<100 au). For instance, the isolated Bok globule B335 shows WCCC in the outer envelope (~1000 au), while it harbors a hot corino in the central 10 au region (Imai et al. 2016). A similar structure can also be seen in L483 (Oya et al. 2017). Therefore, it is not obvious whether the high ratios observed at a 1000 au scale are brought onto a smaller scale (<100 au), as they are. On the other hand, the WCCC sources L1527 and TMC-1A indeed show faint emission of CH_3OH even at a 100 au scale. Although the chemical composition at a 1000 au scale likely affects that at a smaller scale to some extent, high-resolution observations are essential to confirm the situation for each source.

5. Conclusions

We present the results of an unbiased survey of the chemical composition toward the 36 Class 0 and Class I protostars in the Perseus molecular cloud complex. The results are summarized as follows:

1. Multiple transition lines of C_2H, c-C_3H_2, and CH_3OH were detected toward most of the target sources. The CH_3OH ($J = 5$–4) lines were detected toward 35 sources, the CH_3OH ($J = 2$–1) and the C_2H ($N = 3$–2) lines toward all the sources, and the c-C_3H_2 ($3_{2,1}$–$2_{1,2}$) lines toward 30 sources.
2. A correlation plot between the integrated intensities of the C_2H and CH_3OH lines is prepared for the two cases with and without the wing components. In both cases, no correlation is seen between them. Similarly, no correlation is found between the integrated intensities of the c-C_3H_2 and CH_3OH lines. In contrast, the integrated intensities of the C_2H and c-C_3H_2 lines show a positive correlation, because these two species are thought to be produced through related chemical pathways.
3. The column density ratios of C_2H/CH_3OH show a significant diversity by 2 orders of magnitude. The hot corino sources show the highest ratio, while the WCCC source L1527, employed as a reference, shows the lowest ratio. The ratios of most sources are in between these two distinct cases.
4. The C_2H/CH_3OH ratio does not correlate with the evolutionary indicators (L_{bol}/L_{smm} and T_{bol}), nor the envelope mass. On the other hand, we find that the isolated sources and the sources located in cloud peripheries tend to have chemical characteristics of WCCC (i.e., high C_2H/CH_3OH ratios). In the Perseus molecular cloud complex, the hot-corino-like sources (i.e., low C_2H/CH_3OH ratios) do not exist in such regions, but are concentrated in the central parts of the cluster-forming regions. This result is qualitatively consistent with the idea that the chemical diversity would originate from the different duration times of the starless core phase after the shielding of the interstellar UV radiation.
5. It is important to study, with high angular resolution observations, whether the chemical composition seen in this study is brought into inner-envelope/disk systems for each source.

We thank the referee for the thoughtful and constructive comments. We are grateful to the staff of NRO and IRAM for excellent support of our observations. This study is supported by KAKENHI (25108005 and 16H03964). The authors also acknowledge financial support by JSPS and MAEE under the Japan-France integrated action programme.

Software: NEWSTAR, GILDAS.

ORCID iDs

Aya E. Higuchi https://orcid.org/0000-0002-9221-2910
Nami Sakai https://orcid.org/0000-0002-3297-4497
Yoshimasa Watanabe https://orcid.org/0000-0002-9668-3592
Yoko Oya https://orcid.org/0000-0002-0197-8751
Muneaki Imai https://orcid.org/0000-0002-5342-6262
Yichen Zhang https://orcid.org/0000-0001-7511-0034
Cecilia Ceccarelli https://orcid.org/0000-0001-9664-6292
Claudio Codella https://orcid.org/0000-0003-1514-3074
Rafael Bachiller https://orcid.org/0000-0002-5331-5386
Tomoya Hirota https://orcid.org/0000-0003-1659-095X
Takeshi Sakai https://orcid.org/0000-0003-4521-7492

References

Bachiller, R., Codella, C., Colomer, F., Liechti, S., & Walmsley, C. M. 1998, A&A, 335, 266
Bachiller, R., & Pérez Gutiérrez, M. 1997, ApJL, 487, L93
Bizzocchi, L., Caselli, P., Spezzano, S., & Leonardo, E. 2014, A&A, 569, A27
Bottinelli, S., Ceccarelli, C., Neri, R., et al. 2004, ApJL, 617, L69
Buckle, J. V., & Fuller, G. A. 2002, A&A, 381, 77
Burke, J. R., & Hollenbach, D. J. 1983, ApJ, 265, 223
Cazaux, S., Tielens, A. G. G. M., Ceccarelli, C., et al. 2003, ApJL, 593, L51
Chen, M. C.-Y., Di Francesco, J., Johnstone, D., et al. 2016, ApJ, 826, 95
Codella, C., Ceccarelli, C., Cabrit, S., et al. 2016, A&A, 586, L3
Cuadrado, S., Goicoechea, J. R., Pilleri, P., et al. 2015, A&A, 575, A82
Fontani, F., Palau, A., Busquet, G., et al. 2012, MNRAS, 423, 1691
Fukui, Y., Harada, R., Tokuda, K., et al. 2015, ApJL, 807, L4
Garrod, R. T., & Herbst, E. 2006, A&A, 457, 927
Gerin, M., Kaźmierczak, M., Jastrzebska, M., et al. 2011, A&A, 525, A116
Graninger, D. M., Wilkins, O. H., & Öberg, K. I. 2016, ApJ, 819, 140
Guzmán, V., Pety, J., Gratier, P., et al. 2015, HiA, 16, 593
Hacar, A., Tafalla, M., & Alves, J. 2017, A&A, 606, A123
Hatchell, J., Fuller, G. A., Richer, J. S., Harries, T. J., & Ladd, E. F. 2007, A&A, 468, 1009
Hatchell, J., Richer, J. S., Fuller, G. A., et al. 2005, A&A, 440, 151
Higuchi, A. E., Chibueze, J. O., Habe, A., Takahira, K., & Takano, S. 2014, AJ, 147, 141
Higuchi, A. E., Kurono, Y., Saito, M., & Kawabe, R. 2010, ApJ, 719, 1813
Hirota, T., Bushimata, T., Choi, Y. K., et al. 2008, PASJ, 60, 37
Hirota, T., Honma, M., Imai, H., et al. 2011, PASJ, 63, 1
Imai, M., Sakai, N., Oya, Y., et al. 2016, ApJL, 830, L37
Jørgensen, J. K., Harvey, P. M., Evans, N. J., et al. 2006, ApJ, 645, 1246
Kirk, H., Johnstone, D., & Di Francesco, J. 2006, ApJ, 646, 1009
Koumpia, E., Semenov, D. A., van der Tak, F. F. S., Boogert, A. C. A., & Caux, E. 2017, A&A, 603, A88
Koumpia, E., van der Tak, F. F. S., Kwon, W., et al. 2016, A&A, 595, A51
Kristensen, L. E., van Dishoeck, E. F., van Kempen, T. A., et al. 2010, A&A, 516, A57
Lefloch, B., Bachiller, R., Ceccarelli, C., et al. 2018, MNRAS, 477, 4792
Lindberg, J. E., Charnley, S. B., & Cordiner, M. A. 2016, ApJL, 833, L14
Lindberg, J. E., & Jørgensen, J. K. 2012, A&A, 548, A24
Lindberg, J. E., Jørgensen, J. K., Watanabe, Y., et al. 2015, A&A, 584, A28
Maret, S., Ceccarelli, C., Tielens, A. G. G. M., et al. 2005, A&A, 442, 527
Meixner, M., & Tielens, A. G. G. M. 1993, ApJ, 405, 216

Öberg, K. I., van der Marel, N., Kristensen, L. E., & van Dishoeck, E. F. 2011, ApJ, 740, 14
Oya, Y., Sakai, N., Sakai, T., et al. 2014, ApJ, 795, 152
Oya, Y., Sakai, N., Watanabe, Y., et al. 2017, ApJ, 837, 174
Pety, J., Goicoechea, J. R., Hily-Blant, P., Gerin, M., & Teyssier, D. 2007, A&A, 464, L41
Sakai, N., Ceccarelli, C., Bottinelli, S., Sakai, T., & Yamamoto, S. 2012, ApJ, 754, 70
Sakai, N., Oya, Y., Sakai, T., et al. 2014a, ApJL, 791, L38
Sakai, N., Sakai, T., Hirota, T., et al. 2014b, Natur, 507, 78
Sakai, N., Sakai, T., Hirota, T., Burton, M., & Yamamoto, S. 2009, ApJ, 697, 769
Sakai, N., Sakai, T., Hirota, T., & Yamamoto, S. 2008, ApJ, 672, 371
Sakai, N., Sakai, T., Hirota, T., & Yamamoto, S. 2010, ApJ, 722, 1633
Sakai, N., Sakai, T., & Yamamoto, S. 2006, PASJ, 58, L15
Sakai, N., & Yamamoto, S. 2013, ChRv, 113, 8981
Saruwatari, O., Sakai, N., Liu, S.-Y., et al. 2011, ApJ, 729, 147
Soma, T., Sakai, N., Watanabe, Y., & Yamamoto, S. 2015, ApJ, 802, 74
Spezzano, S., Bizzocchi, S., Caselli, P., Harju, J., & Brünken, S. 2016a, A&A, 592, L11
Spezzano, S., Gupta, H., Brünken, S., et al. 2016b, A&A, 586, A110
Stutzki, J., Stacey, G. J., Genzel, R., et al. 1988, ApJ, 332, 379
Takakuwa, S., Mikami, H., Saito, M., & Hirano, N. 2000, ApJ, 542, 367
Taquet, V., Ceccarelli, C., & Kahane, C. 2012, A&A, 538, A42
Tielens, A. G. G. M., & Hagen, W. 1982, A&A, 114, 245
Watanabe, N., & Kouchi, A. 2002, ApJL, 571, L173
Watanabe, Y., Sakai, N., Lindberg, J. E., et al. 2012, ApJ, 745, 126
Watanabe, Y., Sakai, N., López-Sepulcre, A., et al. 2015, ApJ, 809, 162
Yamaguchi, T., Takano, S., Watanabe, Y., et al. 2012, PASJ, 64, 105
Yoshida, K., Sakai, N., Tokudome, T., et al. 2015, ApJ, 807, 66
Yamamoto, S. 2017, Introduction to Astrochemistry: Chemical Evolution from Interstellar Clouds to Star and Planet Formation (Tokyo: Springer Japan)